J. Mech. Phys. Solids 146 (2021) 104196

Contents lists available at ScienceDirect

Journal of the Mechanics and Physics of Solids

journal homepage: www.elsevier.com/locate/jmps

Non-reciprocal Rayleigh wave propagation in space–time modulated surface

Qian Wu, Hui Chen, Hussein Nassar, Guoliang Huang *

Department of Mechanical and Aerospace Engineering, University of Missouri, Columbia, MO 65211, USA

ARTICLE INFO

Keywords:
Space–time modulation
Rayleigh waves
Coupled mode theory
Non-reciprocity
One-way mode conversion

ABSTRACT

Research on non-reciprocal propagation of waves is of great significance in the field of photonic and phononic crystals for realizing flexible one-way propagation devices with potential engineering applications. Here, non-reciprocal Rayleigh waves are investigated in a continuous two-dimensional (2D) semi-infinite medium bound with an array of space–time modulated spring–mass oscillators. The involved modulation is a wave-like perturbation of the surface of the continuous medium that breaks time-reversal symmetry and reciprocity. To characterize the propagation of Rayleigh waves in such a complex 2D medium with continuous and discrete interface, an analytical study is performed to obtain dispersion-engineered bandgaps by adopting the asymptotic method and coupled mode theory, which is also validated by numerical simulation. Specifically, the non-reciprocal transmission of Rayleigh waves with one-way mode conversion is illustrated, and various relevant physical quantities, including conversion length and band gap size, are quantitatively estimated. This work sheds light on versatile control of Rayleigh wave propagation ranging from sensing and evaluation of engineering structures to guided wave-based damage detection techniques.

0. Introduction

Rayleigh waves, discovered in 1885 by Lord Rayleigh, are a type of Surface Acoustic Waves (SAWs) that propagate over relatively long distances at the free surfaces of solids with amplitudes exponentially decaying perpendicular to the surfaces. Research on effectively controlling and manipulating Rayleigh waves has been gathering great attention from both scientific and engineering communities for decades. Several well-studied strategies have been proposed across multiple research fields involving designs of distributions of simple artificial micro- and macro-structures such as pillars, grooves, resonators, etc, on the surface of the host medium (Ash et al., 2017; Benchabane et al., 2017; Boechler et al., 2013; Khelif et al., 2010; Wu et al., 2004; Colquitt et al., 2017; Zhu et al., 2015; Badreddine Assouar and Oudich, 2011; Wu et al., 2008; Li et al., 2018). Advantages of doing so are twofold. First, the existence of these external inclusions does not require any modification on the geometrical or material properties of the continuum, keeping the host media intact. Second, tunable features can be easily realized in experimental implementations. As an outstanding example, the use of phononic crystals and mechanical metamaterials provides extra degree of freedom in tailoring the propagating behaviors of Rayleigh waves, such as scattering performance, polarization control and so on. Further, existing developments in novel SAW devices enable a wide range of applications in sensing (Liu et al., 2016; Devkota et al., 2017; Polewczyk et al., 2017; Kadota et al., 2011; Aubert et al., 2010; Delsing et al., 2019), rf filters (Ruppel, 2017), duplexers (Kadota et al., 2005) and seismic wave mitigation (Colquitt et al., 2017; Colombi et al., 2016; Artru et al., 2004).

* Corresponding author.
E-mail address: huangg@missouri.edu (G. Huang).

https://doi.org/10.1016/j.jmps.2020.104196
Received 28 June 2020; Received in revised form 11 October 2020; Accepted 14 October 2020
Available online 17 October 2020

Nomenclature

$\boldsymbol{\varphi}$	Mode shape of Rayleigh wave in the semi-infinite medium
$\boldsymbol{F}$, $\boldsymbol{G}$, $\boldsymbol{H}$, $\boldsymbol{I}$	Modulation induced effective body forces
$\cdot^*$	Complex conjugate
$\cdot^j$, $\cdot_j$	jth-order harmonic terms. In this work, $j = -1$, 0, or 1
$\delta\cdot$	First-order correction terms
$\langle\cdot\rangle$	Averaging operator $\langle\cdot\rangle \equiv 1/2\pi \int_0^{2\pi}$
μ, λ	Lamé constants
Ω	Resonance frequency of the unperturbed oscillator $\Omega = \sqrt{K/m}$
∂_i	Partial differential operator with respect to i
$\boldsymbol{\Phi}$, $\boldsymbol{\Psi}$	Unperturbed scalar and vector potential functions
ρ	Mass density of the semi-infinite host medium
$\widetilde{\cdot}$	Perturbed terms
$\widetilde{U}$, $\widetilde{W}$	Magnitudes of the perturbed x- and z-directional displacements in the semi-infinite medium
ξ	Phase term of the modulation $\xi = q_m x - \omega_m t$
c_T, c_L, c_R	Phase velocities for transverse, longitudinal, and Rayleigh waves
D_1, D_2	Magnitudes of the unperturbed scalar and vector potential functions
K_m, K, δK	Modulated spring constant, unmodulated spring constant, and modulation strength of the spring constant
m, A, l_s	Mass, occupied area, and spacing of each individual spring–mass oscillator
Q	Normalized wavenumber $Q = 2 \times 10^5$ m^{-1}
q_m, ω_m, v_m, λ_m	Modulation wavenumber, angular frequency, speed, and wavelength
r_j, p_j, s_j	Dimensionless terms of jth-order harmonic. $r_j = 2-\omega_j^2/c_T^2 q_j^2$, $p_j = \sqrt{1-\omega_j^2/c_L^2 q_j^2}$, and $s_j = \sqrt{1-\omega_j^2/c_T^2 q_j^2}$
u, w, Z	Unperturbed x-directional, z-directional displacements in the semi-infinite medium, and unperturbed mass displacement of the oscillator
V_0, V_1	Amplitudes for fundamental and first-order harmonics chosen by linearity

Despite decades of research on the manipulation of Rayleigh waves, most studies are by far focused on reciprocal systems with time-reversal symmetry, where scattering does not necessarily rely on propagation sense. To break time-reversal symmetry, a novel class of materials, called dynamic or spatio-temporal materials (Lurie, 1997), in the fields of acoustics and elasticity have been vastly investigated in both discrete and continuous systems. This type of materials features properties which not only change in space but also in time in a wave-like fashion referred to as a "pump wave". Recent studies have theoretically and numerically unveiled unprecedented wave-transmission behavior in dynamic materials (Nassar et al., 2017a,b,c; Wallen and Haberman, 2019; Yi et al., 2017; Nassar et al., 2020). Examples of applications include the realization of directional mode converters (Yu and Fan, 2009; Zanjani et al., 2014), selective acoustic circulators (Fleury et al., 2014), directional wave reflectors (Trainiti and Ruzzene, 2016; Swinteck et al., 2015) and directional wave accelerators (Nassar et al., 2017c). However, to the best of our knowledge, little to no theoretical work has been conducted on realizing non-reciprocal propagation of Rayleigh waves with space–time modulations.

In this paper, we perform an extensive study of Rayleigh wave propagation in a 2D semi-infinite medium bound by an array of space–time modulated spring–mass oscillators. Note that as suggested by Casadei et al. (2012) and Chen et al. (2014, 2019), modulating the stiffness of oscillators is technologically feasible using programmable piezoelectric components. To characterize the propagation of Rayleigh waves in the medium involving both continuous and discrete interfaces, we develop the analytical model by using asymptotic method and coupled mode theory to obtain modified dispersion relations of the Rayleigh wave due to the wave-like modulation. Theoretical findings for non-reciprocal wave transmission are validated by transient numerical simulations. Specifically, one-way wave mode conversion is quantitatively characterized. Various relevant physical quantities, such as gap widths and interaction lengths, are estimated so as to guide future experimental implementations. This study can lead to further advance of Rayleigh wave-based devices to enable asymmetric propagation of energy, topological insulators and one-way waveguiding.

1. Theoretical modeling

1.1. Rayleigh wave dispersion in space–time modulated media

We start with a brief review of Rayleigh wave solution in a 2D isotropic semi-infinite medium. In that context, the governing Navier's equations are expressed as

$$[(2\mu+\lambda)\,\partial_x^2 + \mu\partial_z^2]u + (\mu+\lambda)\,\partial_x\partial_z w = \rho\partial_t^2 u \tag{1}$$

$$(\mu+\lambda)\,\partial_x\partial_z u + [(2\mu+\lambda)\,\partial_z^2 + \mu\partial_x^2]w = \rho\partial_t^2 w \tag{2}$$

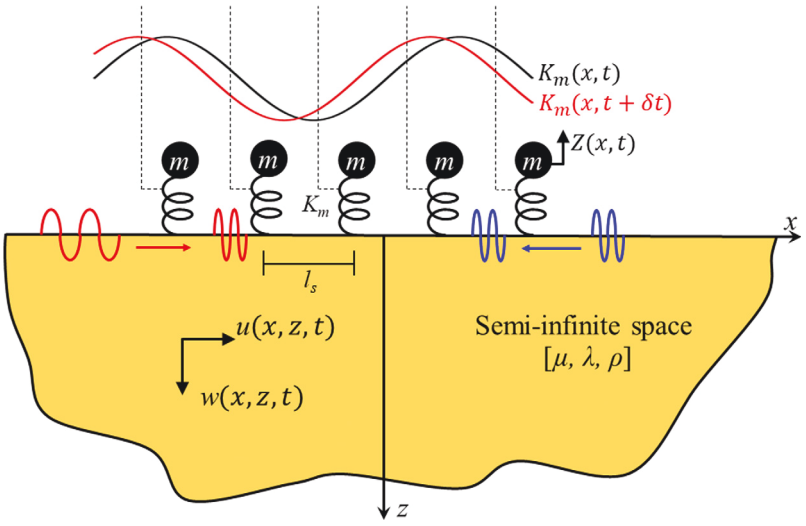

Fig. 1. Schematic of non-reciprocal propagation of Rayleigh waves at the space–time modulated surface of a semi-infinite medium. An array of oscillators, including masses m and modulated spring constants $K_m(x,t) = K + \delta K \cos(q_m x - \omega_m t)$ with K being unperturbed spring constant, are attached to the surface of the medium. Each of the oscillators is separated with one another by a spacing l_s. The oscillators only vibrate along the z-direction. The isotropic continuous medium is described by a set of elastic parameters (μ, λ and ρ). The Rayleigh waves propagate at the surface in a non-reciprocal way that the transmission or reflection depends on directions of incidence at specific frequencies.

where μ and λ denote Lamé constants of the medium and u and w represent the displacement fields along the $x-$ and $z-$directions, respectively. Operator ∂_i with i denoting x, z or t is a partial derivative operator with respect to i, and will be used throughout the paper. By introducing the potentials $u = \partial_x \Phi + \partial_z \Psi$ and $w = \partial_z \Phi - \partial_x \Psi$, the Navier's Eqs. (1) and (2) are reformulated as

$$\nabla^2 \Phi - \frac{1}{c_L^2} \partial_t^2 \Phi = 0 \tag{3}$$

$$\nabla^2 \Psi - \frac{1}{c_T^2} \partial_t^2 \Psi = 0 \tag{4}$$

where $c_L = \sqrt{\lambda + 2\mu/\rho}$ and $c_T = \sqrt{\mu/\rho}$ are the phase velocities for longitudinal (L) and transverse (T) waves. By solving Eqs. (3) and (4) and applying stress conditions at the free boundary: $\sigma_{zz} = \sigma_{xz} = 0$, the non-dispersive Rayleigh wave solution at the free surface can be obtained as

$$\Phi = D_1(z) \exp\left[i\left(q_0 x - \omega_0 t\right)\right] \tag{5}$$

$$\Psi = D_2(z) \exp\left[i\left(q_0 x - \omega_0 t\right)\right] \tag{6}$$

where q_0 is the wave-number along x-axis and ω_0 is angular frequency.

In the study that follows, instead of the above free surface, we will consider Rayleigh wave propagation at a space–time modulated surface by introducing an array of linear oscillators connected at the surface to the semi-infinite medium, as shown in Fig. 1. Each linear oscillator is composed of a mass m and spring constant K and the spacing between oscillators is set to be l_s. Now a wave-like modulation on the spring constant is assumed as $K_m = K + \delta K \cos(q_m x - \omega_m t) = K + \delta K(\xi)$, with δK, q_m and ω_m being the modulation amplitude, modulation wavenumber and modulation frequency, respectively. The modulation wavelength can be subsequently defined as $\lambda_m = 2\pi/q_m$. The modulation amplitude δK is assumed to be small compared with K but great enough to break reciprocity.

The perturbative approach based on the amplitude of the modulation then is utilized to investigate how an incident Rayleigh wave is transformed by the modulation (Nassar et al., 2017a,b,c). In the presence of perturbation, the governing equations (1) and (2) are modified accordingly as

$$[(2\mu + \lambda)\partial_x^2 + \mu\partial_z^2]\widetilde{u} + (\mu + \lambda)\partial_x \partial_z \widetilde{w} = \rho \partial_t^2 \widetilde{u} \tag{7}$$

$$(\mu + \lambda)\partial_x \partial_z \widetilde{u} + [(2\mu + \lambda)\partial_z^2 + \mu\partial_x^2]\widetilde{w} = \rho \partial_t^2 \widetilde{w} \tag{8}$$

where $\widetilde{u} = u_0 + \delta u + \cdots$ and $\widetilde{w} = w_0 + \delta w + \cdots$. The perturbed potential functions can be written as

$$\widetilde{\Phi} = \widetilde{D}_1(\xi, z)\, e^{i(\widetilde{q}x - \widetilde{\omega}t)} \tag{9}$$

$$\widetilde{\Psi} = \widetilde{D}_2(\xi, z)\, e^{i(\widetilde{q}x - \widetilde{\omega}t)} \tag{10}$$

in which $\widetilde{q} = q_0 + \delta q + \cdots$, $\widetilde{\omega} = \omega_0 + \delta\omega + \cdots$, and $\widetilde{D}_i = D_i + \delta D_i + \cdots$, and δq, $\delta\omega$ and δD_i are the first-order correction terms to q_0, ω_0 and D_i, respectively. According to the Bloch theorem, the two potential functions are 2π-periodic functions of ξ. Therefore, we

can decompose the leading-order amplitude of the potential function into $D_1(\xi, z) = \sum_{j\in\mathbb{Z}} D_1^j(z)e^{ij\xi}$, where j denotes the Fourier order and $\mathbb{Z}$ denotes the collection of integer numbers. By keeping the terms of leading-order correction and considering only the jth-order harmonic component, substituting Eq. (9) into the perturbed equations (3) and (4) leads to

$$\partial_z^2 D_1^j(z) + \left(\omega_j^2/c_L^2 - q_j^2\right) D_1^j(z) = 0 \tag{11}$$

$$\partial_z^2 D_2^j(z) + \left(\omega_j^2/c_T^2 - q_j^2\right) D_2^j(z) = 0 \tag{12}$$

where $\omega_j = \omega_0 + j\omega_m$ and $q_j = q_0 + jq_m$. On the other hand, the equation of motion of surface oscillators can be written as

$$m\partial_t^2 Z^j + K_m\left(Z^j - w_{z=0}^j\right) = 0 \tag{13}$$

where Z^j is the jth-order harmonic component of the mass displacement up to the leading-order correction. We assume a traveling wave solution reading $Z = \sum_{j\in\mathbb{Z}} Z_0^j e^{ij\xi}e^{i(\tilde{q}x-\tilde{\omega}t)}$ for the oscillator mass motion and keep only the leading-order terms. Following the supplementary material of Boechler et al. (2013) and the process detailed in Appendix A, we obtain the characteristic equation of leading-order correction which describes the Rayleigh wave dispersion in the presence of space–time modulated oscillators.

$$\left(\frac{m\omega_j^2}{K} - 1\right)\left[\left(2 - \frac{\omega_j^2}{q_j^2c_T^2}\right)^2 - 4\sqrt{1 - \frac{\omega_j^2}{q_j^2c_T^2}}\sqrt{1 - \frac{\omega_j^2}{q_j^2c_L^2}}\right] = \frac{m}{A\rho}\frac{\omega_j^4}{q_j^3c_T^4}\sqrt{1 - \frac{\omega_j^2}{q_j^2c_L^2}} \tag{14}$$

This equation is exactly the one obtained in Boechler et al. (2013), but with higher-order terms. For the Rayleigh wave propagating along $-x$ direction, the dispersion relation can be easily obtained by conducting similar derivation theretofore. Moreover, we can define an eigenmode $\boldsymbol{\varphi}^j(\omega_j, q_j)$ which describes the mode shape of Rayleigh waves in the presence of the spring–mass oscillators by matching the stress conditions as

$$\boldsymbol{\varphi}^j(\omega_j, q_j) = \begin{bmatrix} u^j \\ w^j \end{bmatrix} = \begin{bmatrix} iq_j(e^{-q_jp_jz} - 2\frac{s_jp_j}{r_j}e^{-q_js_jz}) \\ -q_jp_j(e^{-q_jp_jz} - \frac{2}{r_j}e^{-q_js_jz}) \end{bmatrix} \tag{15}$$

where $r_j = 2 - \omega_j^2/c_T^2q_j^2$, $p_j = \sqrt{1 - \omega_j^2/c_L^2q_j^2}$, and $s_j = \sqrt{1 - \omega_j^2/c_T^2q_j^2}$. The displacement of the oscillator mass Z_0^j accordingly reads

$$Z_0^j = \frac{\Omega^2 q_j p_j}{\omega_j^2 - \Omega^2}\left(1 - \frac{2}{r_j}\right) \tag{16}$$

where $\Omega = \sqrt{K/m}$ represents the resonant frequency of the unperturbed oscillators. The dispersion diagram is calculated in Fig. 2 from Eq. (14) for j equal to 0 and ±1. In general, when the pump wave has its first N Fourier components non-zero, j can take integer values between $-N$ and N. The hatched area represents the bulk modes which mainly survive in the bulk region of the semi-infinite medium and hence are of less interest in this work. For the fundamental harmonic $\boldsymbol{\varphi}^0(\omega_0, q_0)$ in absence of modulation, a large band gap generated by the local resonance of oscillators can be witnessed. The lower branch goes towards the resonance frequency Ω as q increases, while the upper branch approaches gradually the non-dispersive Rayleigh dispersion curve ($\omega = c_Rq$) which is not shown here. With modulation turned on, the first-order harmonics $\boldsymbol{\varphi}^{-1}(\omega_{-1}, q_{-1})$ and $\boldsymbol{\varphi}^1(\omega_1, q_1)$ appear with linear shifts of dispersion curves, with respect to the fundamental mode $\boldsymbol{\varphi}^0$. In Fig. 2, points of no-intersection correspond to uncoupled cases in which only mode $\boldsymbol{\varphi}^0$ exists, leading to the eigenmode

$$\boldsymbol{\varphi}(\xi) = V_0\boldsymbol{\varphi}^0 \tag{17}$$

where V_0 is the linear amplitude of $\boldsymbol{\varphi}^0$. This means physically that the incident mode $\boldsymbol{\varphi}^0$ will not get scattered while propagating in the space–time modulated area. On the other hand, points of intersections $\boldsymbol{\varphi}^0 \cap \boldsymbol{\varphi}^{\pm1}$ correspond to coupled cases where more than one eigenmodes exist. Accordingly, the eigenmode reads

$$\boldsymbol{\varphi}(\xi) = V_0\boldsymbol{\varphi}^0 + V_{\pm1}\boldsymbol{\varphi}^{\pm1}e^{\pm i\xi} \tag{18}$$

which is the sum of a pair of coupled modes with the amplitudes V_0 and $V_{\pm1}$ respectively.

Fig. 2 graphically illustrates three pairs of coupled modes denoted as A, B and C. Taking pair A as an example, if one leg, say $\boldsymbol{\varphi}^0 \cap \boldsymbol{\varphi}^1$, is incident from left, the other leg, $\boldsymbol{\varphi}^0 \cap \boldsymbol{\varphi}^{-1}$, is scattered and also propagates along the $-x$-direction. On the other hand, $\boldsymbol{\varphi}^0 \cap \boldsymbol{\varphi}^1$ will not be scattered when incident from right. This indicates the non-reciprocal propagation of Rayleigh waves at our space–time modulated surface. In general, when the Rayleigh wave excited at any of the coupled modes from certain direction is scattered, it will not be scattered from the opposite direction. This is a direct consequence of the existence of space–time modulation which breaks the time-reversal symmetry. With the current parameters, following Mace and Manconi (2012), pairs A and B correspond to veering pairs where the two interacting branches veer without the formation of directional bandgap (scattering and incidence in the same direction, and the group velocities of the two branches hold the identical sign), whereas pair C is a locking pair because the two interacting branches now lock around a directional bandgap (scattering and incidence in the opposite directions, and the

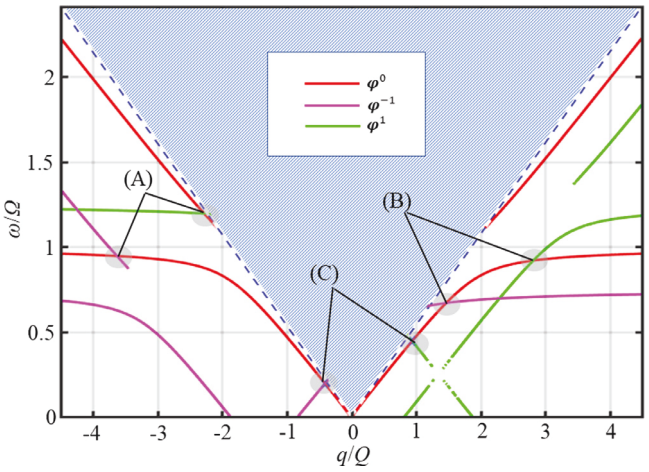

Fig. 2. Coupling and non-reciprocity: A breaking of time-reversal symmetry produces three pairs of coupled modes (A), (B) and (C). Pairs (A) and (B) manifest as veering pairs, while pair (C) is the locking one. The pattern-hatched area represents the region of bulk modes, enclosed by a shear-wave cone (blue dashed). The constitutive parameters used here are set as $\rho = 2.2$ g/cm^3, $\lambda = 12.354$ GPa, $\mu = 28.826$ GPa, $K = 2400$ N/m, $m = 1.315 \times 10^{-15}$ kg, and $A = 1.0101 \times 10^{-12}$ m^2. ω is normalized to the resonance frequency of oscillators $\Omega = \sqrt{K/m}$ while q is normalized to $Q = 2 \times 10^5$ m^{-1}. The modulation parameters throughout the paper are selected as $\omega_m = \Omega/4$ and $q_m = 1.35Q$.

group velocities of the interacting branches hold the opposite signs). It is worth noting that the non-reciprocity here only occurs in a narrow band of frequencies for given surface parameters. That being said, excitation far away from these non-reciprocal pairs on the dispersion curve will only yield fundamental harmonic wave whose frequency and wavenumber remain on the fundamental dispersion curve. To achieve broadband non-reciprocity, one may consider the possible approach of utilizing active circuit control to modify the modulation parameters of the surface oscillators in real-time (Chen et al., 2019). Careful observation reveals that the dispersion curves for $\boldsymbol{\varphi}^{-1}$ and $\boldsymbol{\varphi}^{1}$ are truncated, as shown in Fig. 2, because Eq. (14) can only capture the propagating details of Rayleigh waves. To further determine the coupling between coupled modes at the points of intersections, the perturbation method for displacement fields of the modulated system will be conducted (Nassar et al., 2017a,c).

1.2. Orthogonality condition of modulated Rayleigh wave propagation

To further determine coupling of coupled modes at the intersection points of the perturbed system involving both the continuous and discrete parts, we assume a set of perturbed plane waves along x-direction in terms of displacement fields as

$$\begin{aligned}
\widetilde{u}(x,z,\xi) &= \widetilde{U}(\xi,z)e^{i(\widetilde{q}_x x-\widetilde{\omega}t)}\\
\widetilde{w}(x,z,\xi) &= \widetilde{W}(\xi,z)e^{i(\widetilde{q}_x x-\widetilde{\omega}t)}\\
\widetilde{Z}(x,z,\xi) &= \widetilde{Z}(\xi)e^{i(\widetilde{q}_x x-\widetilde{\omega}t)}
\end{aligned} \tag{19}$$

where $\widetilde{U} = u + \delta u$, $\widetilde{W} = w + \delta w$, $\widetilde{q}_x = q_0 + \delta q$, $\widetilde{Z} = Z_0 + \delta Z$ and $\widetilde{\omega} = \omega_0 + \delta\omega$, up to first-order corrections. Substituting Eq. (19) into the governing equations (7), (8) and the perturbed equation (13) and keeping only the first-order correction terms yields a new set of governing equations for the forced wave propagation.

$$\begin{bmatrix} (2\mu+\lambda)\left(iq_0+q_m\partial_\xi\right)^2+\mu\partial_z^2 & (\mu+\lambda)\left(iq_0+q_m\partial_\xi\right)\partial_z \\ (\mu+\lambda)\left(iq_0+q_m\partial_\xi\right)\partial_z & (2\mu+\lambda)\partial_z^2+\mu\left(iq_0+q_m\partial_\xi\right)^2 \end{bmatrix}\delta\boldsymbol{\varphi} + \boldsymbol{F} = \rho(i\omega_0+\omega_m\partial_\xi)^2\delta\boldsymbol{\varphi} \tag{20}$$

$$-K\left(\delta Z-\delta w_{z=0}\right)+G = m\left(i\omega_0+\omega_m\partial_\xi\right)^2\delta Z \tag{21}$$

where $\delta\boldsymbol{\varphi} = (\delta u, \delta w)^T$. The above equations describe the first-order correction terms, i.e. δu, δw and δZ, propagating at the space–time modulated surface. The corresponding stress boundary conditions of first-order corrections at z =0 now become

$$\left[\mu\left(iq_0+q_m\partial_\xi\right)\delta w+\mu\partial_z\delta u\right]_{z=0} = H \tag{22}$$

$$\left[\lambda\left(iq_0+q_m\partial_\xi\right)\delta u+(2\mu+\lambda)\partial_z\delta w\right]_{z=0} = -\frac{K}{A}\left(\delta Z-\delta w_{z=0}\right)+I \tag{23}$$

Here, we obtain a set of modulation-induced effective body forces of the first-order correction, reading

$$\boldsymbol{F} = \begin{bmatrix}\alpha\\ \beta\end{bmatrix} \tag{24}$$

$$G = -\delta K_m(\xi)\left(Z - w_0\right) + m\left(2\omega_0\delta\omega - 2i\delta\omega\omega_m\partial_\xi\right)Z \tag{25}$$

$$H = -i\mu\delta q w_{z=0} \tag{26}$$

$$I = -\frac{\delta K(\xi)}{A}\left(Z - w_{z=0}\right) - i\lambda\delta q u_{z=0} \tag{27}$$

where

$$\alpha = [(2\mu+\lambda)\left(-2q_0\delta q + 2iq_m\delta q\partial_\xi\right) + \rho\left(2\omega_0\delta\omega - 2i\delta\omega\omega_m\partial_\xi\right)]u + i\left(\mu+\lambda\right)\delta q\partial_z w$$

$$\beta = [\mu\left(-2q_0\delta q + 2iq_m\delta q\partial_\xi\right) + \rho\left(2\omega_0\delta\omega - 2i\delta\omega\omega_m\partial_\xi\right)]w + i\left(\mu+\lambda\right)\delta q\partial_z u.$$

Expressions (24)–(27) are functions of δq, $\delta\omega$ and δK. Among them, expression (24) corresponds to the effective body force applied on the continuum, while expression (25) represents the effective body force applied on the discrete spring–mass oscillator section.

In deriving the orthogonality condition, the effective body force in the continuum is coupled with the one in the discrete section through the stress boundary conditions of first-order corrections. The orthogonality condition requires all the effective body forces to do zero virtual work for all the possible eigenmodes (Nassar et al., 2017a,b,c). By following the detailed derivation in Appendix B, we reach eventually the orthogonality condition relating the continuous and discrete sections:

$$w^*_{z=0}\left(\frac{Q_0}{A}\langle G\rangle - \langle I\rangle\right) - u^*_{z=0}\langle H\rangle + \int_0^\infty \boldsymbol{\varphi}^*\cdot\langle \boldsymbol{F}\rangle\, dz = 0 \tag{28}$$

where $Q_j = 1 - m\omega_j^2/(m\omega_j^2 - K)$, $j\in\mathbb{Z}$. Eq. (28) indicates the virtual work done by the effective body forces G, I, H and $\boldsymbol{F}$ is zero. In other words, the body forces have to be perpendicular to the eigenvector in a way to avoid increasing and unbounded oscillating amplitudes in the system (Nassar et al., 2017a,b,c). Based on the derived orthogonality condition of our spring–mass-decorated system, we can further examine the couplings between the coupled modes.

1.3. Uncoupled mode

We first consider the case of a lonely uncoupled mode. Without loss of generality, the considered harmonic here is chosen to be the fundamental mode $\boldsymbol{\varphi}^0\left(q_0,\omega_0\right)$. Combining Eqs. (15), (16), (17) and (24)–(27) and taking average on the resulting equations basically yields a set of averaged effective body forces for $\boldsymbol{\varphi}^0$

$$\begin{aligned}
\langle \boldsymbol{F}\rangle^0 &= \begin{bmatrix} V_0\left[-2q_0\delta q\left(2\mu+\lambda\right) + 2\rho\omega_0\delta\omega\right]u^0 + i\left(\mu+\lambda\right)\delta q\partial_z V_0 w^0 \\ V_0\left[-2\mu q_0\delta q + 2\rho\omega_0\delta\omega\right]w^0 + i\left(\mu+\lambda\right)\delta q\partial_z V_0 u^0 \end{bmatrix} \\
\langle G\rangle^0 &= 2m\omega_0\delta\omega V_0 Z^0 \\
\langle H\rangle^0 &= -i\mu\delta q V_0 w^0_{z=0} \\
\langle I\rangle^0 &= -i\lambda\delta q V_0 u^0_{z=0}
\end{aligned} \tag{29}$$

Here, the amplitude V_0 can be chosen arbitrarily by linearity. Substituting Eqs. (29) into Eq. (28) results in

$$\mathcal{I}^0 + i\mu\delta q w^0_{z=0}u^{0*}_{z=0} + w^{0*}_{z=0}\left(\frac{2}{A}m\omega_0\delta\omega Q_0 Z^0 + i\lambda\delta q u^0_{z=0}\right) = 0 \tag{30}$$

where the integration reads $\mathcal{I}^j = \frac{1}{V_j}\int_0^\infty \boldsymbol{\varphi}^{j*}\cdot\langle\boldsymbol{F}\rangle^j\, dz$, $j\in\mathbb{Z}$. Using the mode shapes in Eqs. (15) and (16) into Eq. (30) and performing rearrangements yields the group velocity of Rayleigh waves for uncoupled modes in presence of modulated spring–mass oscillators.

$$v_g^0 = \frac{\delta\omega}{\delta q} = -\frac{a_0}{b_0} \tag{31}$$

where a_j and $b_j, j\in\mathbb{Z}$ are functions of ω_j, q_j, K and m, and are detailed in Appendix C. Alternatively, the expression of the group velocity can also be derived from a variation of the dispersion relation in Eq. (14).

1.4. Coupled mode

Then, we investigate the coupling between two harmonics at mode $\boldsymbol{\varphi}^0\cap\boldsymbol{\varphi}^1$, which corresponds to the simplest case. We will first discuss the veering pairs (pairs A and B in Fig. 2), since the coupled modes involved have the wavenumbers of identical sign. In this way, the mode shape in the continuous medium takes the form (18) while that in the discrete section is changed accordingly as

$$Z^j = \frac{\Omega^2 q_j p_j}{\omega_j^2 - \Omega^2}\left(1 - \frac{2}{r_j}\right),\ j = \pm 1 \tag{32}$$

Substituting the mode shape (18) into the effective body forces (24)–(27) results in a new set of effective body forces for the coupled modes.

$$\begin{aligned}
\boldsymbol{F} &= \begin{bmatrix}\alpha\\ \beta\end{bmatrix}\\
G &= -\delta K(\xi)(V_0 Z^0 + V_1 Z^1 e^{i\xi} - V_0 w^0_{z=0} - V_1 w^1_{z=0} e^{i\xi})\\
&\quad + 2m\omega_0\delta\omega V_0 Z^0 + 2m\omega_1\delta\omega V_1 Z^1 e^{i\xi}\\
H &= -i\mu\delta q(V_0 w^0_{z=0} + V_1 w^1_{z=0} e^{i\xi})\\
I &= \frac{\delta K(\xi)}{A}(V_0 Z^0 + V_1 Z^1 e^{i\xi} - V_0 w^0_{z=0} - V_1 w^1_{z=0} e^{i\xi})\\
&\quad - i\lambda\delta q(V_0 u^0_{z=0} + V_1 u^1_{z=0} e^{i\xi})
\end{aligned} \tag{33}$$

where

$$\begin{aligned}
\alpha &= V_0[-2q_0\delta q(2\mu+\lambda) + 2\rho\omega_0\delta\omega]u^0 + V_1[-2q_1\delta q(2\mu+\lambda)\\
&\quad +2\rho\omega_1\delta\omega]u^1 e^{i\xi} + i(\mu+\lambda)\delta q\partial_z(V_0 w^0 + V_1 w^1 e^{i\xi})\\
\beta &= V_0[-2\mu q_0\delta q + 2\rho\omega_0\delta\omega]w^0 + V_1[-2\mu q_1\delta q\\
&\quad +2\rho\omega_1\delta\omega]w^1 e^{i\xi} + i(\mu+\lambda)\delta q\partial_z(V_0 u^0 + V_1 u^1 e^{i\xi})
\end{aligned}$$

Repeating the procedures used in the uncoupled scenario for both the fundamental and first-order harmonics yields

$$\begin{bmatrix}\mathcal{E}_{11} & \mathcal{E}_{12}\\ \mathcal{E}_{21} & \mathcal{E}_{22}\end{bmatrix}\begin{bmatrix}V_0\\ V_1\end{bmatrix} = \mathcal{E}\begin{bmatrix}V_0\\ V_1\end{bmatrix} = 0 \tag{34}$$

where

$$\begin{aligned}
\mathcal{E}_{11} &= a_0\delta q + b_0\delta\omega\\
\mathcal{E}_{12} &= q_0 p_0\frac{\delta K}{A}(1-\frac{2}{r_0})\left(Z^1 + q_1 p_1(1-\frac{2}{r_1})\right)(Q_0+1)\\
\mathcal{E}_{21} &= q_1 p_1\frac{\delta K}{A}(1-\frac{2}{r_1})\left(Z^0 + q_0 p_0(1-\frac{2}{r_0})\right)(Q_1+1)\\
\mathcal{E}_{22} &= a_1\delta q + b_1\delta\omega
\end{aligned} \tag{35}$$

and $\langle\delta K e^{i\xi}\rangle = \langle\delta K e^{-i\xi}\rangle = \delta K$ (also see Appendix D for detailed derivation). Solving the eigenvalue problem $|\mathcal{E}| = \mathbf{0}$ leads to first-order corrections to the dispersion curve around the coupled modes $\boldsymbol{\varphi}^0 \cap \boldsymbol{\varphi}^1$.

$$\delta\omega = \frac{-(a_1 b_0 + a_0 b_1)}{2b_0 b_1}\delta q \pm \frac{1}{2b_0 b_1}\sqrt{(a_1 b_0 - a_0 b_1)^2(\delta q)^2 + 4b_0 b_1 \mathcal{E}_{12}\mathcal{E}_{21}} \tag{36}$$

By picking $\delta K = 0$ (unmodulated scenario), $\mathcal{E}_{12}$ and $\mathcal{E}_{21}$ in Eq. (35) vanish, and the above expression (36) gives the Rayleigh wave group velocities v_g^0 and v_g^1 for the uncoupled modes $\boldsymbol{\varphi}^0$ and $\boldsymbol{\varphi}^1$, respectively. For the non-reciprocal locking pair (pair C in Fig. 2), the two legs are in opposite propagating directions, and hence perform opposite elliptical particle motion directions for the displacement fields. In this way, the expressions of mode shapes of the locking pair need to be accordingly corrected as

$$\begin{aligned}
\boldsymbol{\varphi}^0 &= \begin{bmatrix}u^0\\ w^0\end{bmatrix} = \begin{bmatrix} iq_0(e^{q_0 p_0 z} - 2\frac{s_0 p_0}{r_0}e^{q_0 s_0 z})\\ q_0 p_0(e^{q_0 p_0 z} - \frac{2}{r_0}e^{q_0 s_0 z})\end{bmatrix}\\
\boldsymbol{\varphi}^1 &= \begin{bmatrix}u^1\\ w^1\end{bmatrix} = \begin{bmatrix} iq_1(e^{-q_1 p_1 z} - 2\frac{s_1 p_1}{r_0}e^{-q_1 s_1 z})\\ -q_1 p_1(e^{-q_1 p_1 z} - \frac{2}{r_1}e^{-q_1 s_1 z})\end{bmatrix}\\
Z^j &= \frac{\Omega^2 q_j p_j}{\omega_j^2 - \Omega^2}\left(1-\frac{2}{r_j}\right)
\end{aligned} \tag{37}$$

Substituting expressions (37) into Eqs. (62)–(65) in Appendix D and simply repeating the same procedures of deriving the veering couplings leads to first-order corrections to the dispersion curve of the locking pair. To graphically illustrate the couplings, we plot the first-order corrections to the three pairs and the dispersion curve of the space–time modulated system in Fig. 3, with the same parameters used in plotting Fig. 2 and a non-zero modulation strength $\delta K = 0.1K$. Fig. 3(a–c) illustrate how the first corrections to the dispersion curve unveil the couplings at these three pairs. Taking the veering pair B shown in Fig. 3(b) as an example, when the lower-frequency point of intersection for mode $(0.668\ \Omega, 1.469Q)$ is incident, it will be converted into the other mode $\left(0.668\ \Omega + \omega_m, 1.469Q + q_m\right)$ at higher frequency within an interaction or conversion length which will be discussed later. Generally speaking, the excitation of one of the coupled legs in the space–time modulated medium leads to the creation of the other leg. The conversion, taking place at certain frequencies in certain directions, will not occur in the opposite propagation direction at the same frequency, which shows non-reciprocity due to the loss of time-reversal symmetry. On the other hand, the interacting branches

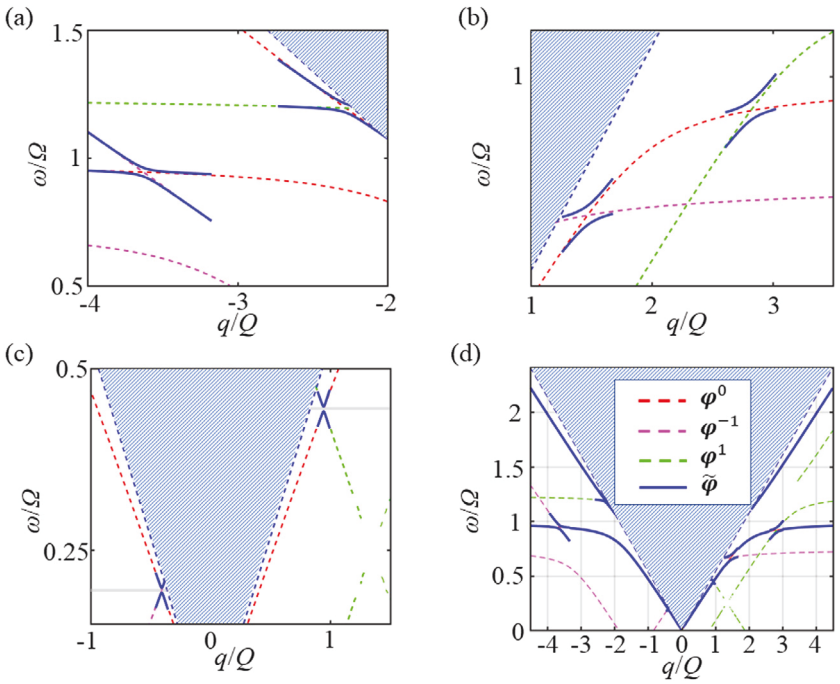

Fig. 3. First-order corrections to the dispersion curve and the corrected dispersion relations up to the first-order correction: A non-zero modulation $\delta K = 0.1K$ enables the couplings between different harmonics. The first-order corrections to the pairs A, B and C in Fig. 2 are illustrated in (a), (b) and (c), respectively. The two shaded areas in (c) represent the two band gaps generated by the modulation. The corrected dispersion curve of the Rayleigh wave propagation in the space–time modulated semi-infinite medium is shown in (d), up to the first-order correction.

of the pairs A and B veer since both coupled modes have the wavenumbers of same signs. There is no band gap formed in the vicinity of them such that the incident waves in principle will not be reflected within the modulation area. Specifically, the upper branch refers to the optical branch where $Z(t)$ and $w_{z=0}(t)$ oscillate out-of-phase, while the lower branch is called acoustic branch where $Z(t)$ and $w_{z=0}(t)$ exhibit in-phase vibration. Pair B exhibits the one-way mode conversion between the acoustic mode and the optical one. By contrast, the two interacting branches of the locking pair C shown in Fig. 2(c) lock and involves two band gaps about the coupled modes. It indicates that any incidence close to one of the coupled modes will be totally reflected into the other one within certain interaction lengths. Following Eq. (36), the veering zone width of frequency $2\delta\omega$ at the critical point ($\delta q = 0$) reads $2\delta\omega(\delta q = 0) = 2\sqrt{b_0 b_1 \mathcal{E}_{12}\mathcal{E}_{21}}/(b_0 b_1)$. We take the two veering pairs in Fig. 3(a) and (b) as an example. The oscillator spacing l_s is solely dependent of the area occupied by the individual oscillator, since we fixed the thickness of the semi-infinite medium. We first plot the intersection frequency and wavenumber of the fundamental and first-order harmonics in function of l_s to show that tuning l_s shifts the spectral location of the intersection of the two veering branches [see Fig. 4(a) and (c)]. As l_s increases, the intersection frequency increases as well as the magnitude of the intersection wavenumber. The veering zone widths $2\delta\omega$ at a certain l_s for both pairs are also plotted in Fig. 4(b) and (d) in functions of l_s and the modulation strength δK. As can be seen, at any l_s, $2\delta\omega$ increases monotonically with the increasing δK. This can be easily concluded from the fact that $\mathcal{E}_{12}$ and $\mathcal{E}_{21}$ are both proportional to δK [see Eq. (35)], which in turn leads $2\delta\omega$ to be proportional to δK as well. On the other side, $2\delta\omega$ is insensitive to the variation of l_s for both veering pairs, at least within the range considered. It is worth mentioning that since our proposed system here is weakly and slowly modulated, i.e. $\delta K \ll K$ and $|\omega_m/q_m| < c_R$, the locking pair is always stable, featuring horizontal directional bandgaps. In strongly modulated systems ($|\omega_m/q_m| > c_R$), it is likely for the system to be unstable to allow the existence of vertical bandgap where the frequency is purely imaginary. Cassedy and Oliner (1963) and Cassedy (1967). Our recent work has already demonstrated the transition from stable to unstable bandgaps when the modulation speed or amplitude in the active system increases (Nassar et al., 2017c). Recent experimental results also proved that the presence of intrinsic losses can quench the instability, making the strongly modulated systems stable (Wang et al., 2018). Lastly, we recover the dispersion curve of Rayleigh waves in the modulated medium in Fig. 3(d). The dashed curves correspond to the uncoupled dispersion curves of fundamental and first-order harmonics. The blue solid curve represents the fixed dispersion diagram up to the first-order correction. In this work, we only consider the first-order correction because it already yields the satisfactory prediction of dispersion curves of coupled modes. Higher-order correction terms may enhance the wave mode coupling shown in Fig. 3 to some degrees. However, their importance can almost be neglected compared with the first-order terms because of the weak modulation considered.

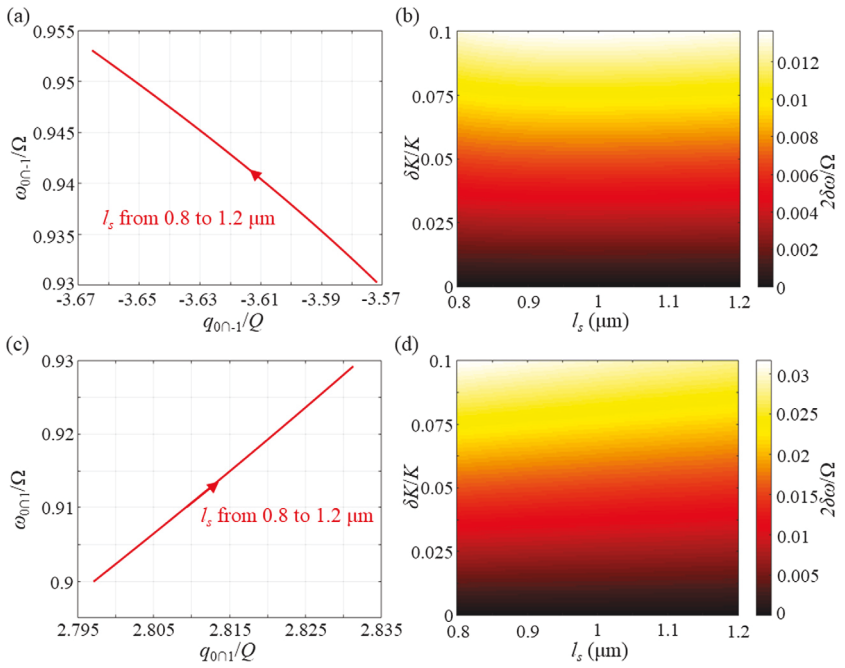

Fig. 4. Parametric study on the influence oscillator spacing ls and modulation strength δK on the intersection frequency and wave number of the fundamental and the first-order harmonics and the veering zone width $2\delta\omega$. (a) and (b) correspond to the veering pair A, while (c) and (d) correspond to the veering pair B. The red arrows in (a) and (c) indicate the increasing direction of l_s.

1.5. Transmission-type conversion

The Rayleigh wave propagating in the space–time modulated medium is converted from one harmonic to one another in the vicinity of the coupled pairs. To characterize their mode conversion properties, we need to discuss separately the veering pairs and locking one. This is simply because the former pairs hold the same signs in group velocity while the latter one is opposite. For the veering pairs, we start by defining the group velocities for the uncoupled harmonics as

$$v_g^0 = -\frac{a_0}{b_0}, \quad v_g^1 = -\frac{a_1}{b_1} \tag{38}$$

Substituting expression (38) into Eq. (36) and utilizing the derivation process detailed in Nassar et al. (2017b) and Appendix E, we can conclude that at the propagation length $d = \pi/(2\delta q_a)$ within the modulated area, where $\delta q_a = \sqrt{\left[\frac{\delta\omega}{2}\left(\frac{1}{v_g^0} - \frac{1}{v_g^1}\right)\right]^2 + \frac{\mathcal{E}_{12}\mathcal{E}_{21}}{b_0 b_1 v_g^0 v_g^1}}$, $\boldsymbol{\varphi}^0$ reaches its minimum while $\boldsymbol{\varphi}^1$ reaches the maximum. Typically, the total conversion from $\boldsymbol{\varphi}^0$ to $\boldsymbol{\varphi}^1$ can be expected when $C_b = 0$, namely, $\delta\omega = 0$. In this case, we have

$$\delta q_\pm = \pm\sqrt{\frac{\mathcal{E}_{12}\mathcal{E}_{21}}{b_0 b_1 v_g^0 v_g^1}}, \quad C_\pm = \pm\frac{b_0 v_g^0}{\mathcal{E}_{12}}\sqrt{\frac{\mathcal{E}_{12}\mathcal{E}_{21}}{b_0 b_1 v_g^0 v_g^1}} \tag{39}$$

For the eigenmode $\boldsymbol{\varphi}^0\,(0.668\ \Omega, 1.469Q)$ corresponding to the veering pair B propagating along the $+x$-direction, we have the normalized conversion length $Qd = 9.56$ and the inverted amplification factor $\frac{1}{|C|} = 0.9726$. To quantitatively illustrate the dependence of Qd and $\frac{1}{|C|}$ on (ω_1, q_1) and the potential tunability of the one-way frequency conversion, we plot in Fig. 5 based on expressions (39) by tuning q_m and ω_m. For a given input mode (ω_0, q_0) marked with yellow pentagrams, the possible output modes are distributed along the dispersion curve of the uncoupled mode (red curves). As can be seen in Fig. 5(a), the closer the coupled mode (ω_1, q_1) is to the resonance frequency of the unmodulated oscillator, the shorter the normalized conversion length appears to be. On the other hand, inverted amplification factor decays as the coupled frequency ω_1 increases. Further, analytical calculations about various combinations of δK and K, shown in Fig. 5(c) and (d), indicate that an increase in δK leads to a decrease in the normalized conversion length Qd when K is fixed. This can be derived from Eqs. (35) and (39) as well. By contrary, when δK is fixed, an increase in K results in an increasing Qd. This behavior is more prominent at larger δK. On the other hand, the variation in δK barely affect the inverted amplification factor $\frac{1}{|C|}$, as can also be observed in Eqs. (35) and (39). However, an increasing K magnifies $\frac{1}{|C|}$.

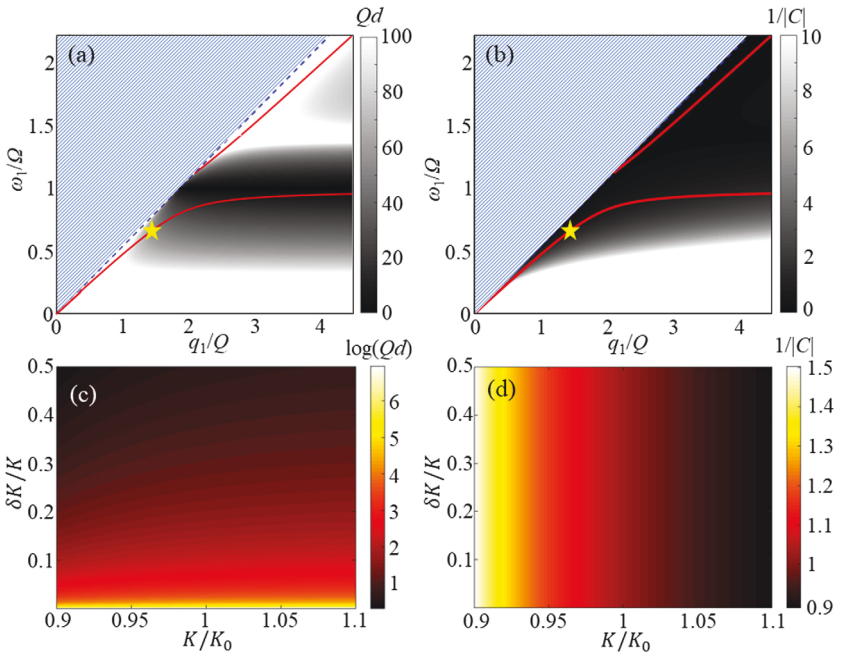

Fig. 5. Dependence of the normalized conversion length Qd (a) and the inverted amplification factor $\frac{1}{|C|}$ (b) on (ω_1, q_1) for an incidence at the mode (ω_0, q_0), marked with yellow pentagrams. The pattern-hatched areas denote the bulk regions, and the red curves are the dispersion curves of the Rayleigh wave in the unmodulated system. (c) and (d) show dependence of log(Qd) and $\frac{1}{|C|}$, respectively, on the variations of K and δK. Here, $K_0 = 2.4 \times 10^3 N/m$.

1.6. Reflection-type conversion

For the locking pair C, the two wavenumbers of the coupled modes are opposite in sign. In this case, reflection-type conversion takes place. Subsequently, expression (69) can be corrected to

$$\delta q_{\pm} = \frac{\delta\omega}{2}\left(\frac{1}{v_g^0} + \frac{1}{v_g^1}\right) \pm i\sqrt{\frac{\mathcal{E}_{12}\mathcal{E}_{21}}{b_0 b_1 v_g^0 v_g^1} - \left[\frac{\delta\omega}{2}\left(\frac{1}{v_g^0} - \frac{1}{v_g^1}\right)\right]^2} = \pm i\delta q_c + \delta q_b \tag{40}$$

As can be seen the first-order correction wavenumber are complex valued in the vicinity of ω_0, specifically for the range

$$|\delta\omega| \le 2\left|\frac{1}{v_g^0} - \frac{1}{v_g^1}\right|^{-1}\sqrt{\frac{\mathcal{E}_{12}\mathcal{E}_{21}}{b_0 b_1 v_g^0 v_g^1}} \tag{41}$$

In this way, the solution for $\boldsymbol{\varphi}^0(\omega_0, q_0)$ incident from the right side is, for $x > 0$,

$$\boldsymbol{\varphi} = V_{0+}e^{-\delta q_c x}\left(\boldsymbol{\varphi}^0 e^{i(q_0 x - \omega_0 t)} + \left(C_a + C_b\right)\boldsymbol{\varphi}^1 e^{i(q_1 x - \omega_1 t)}\right)e^{i(\delta q_b x - \delta\omega t)} \tag{42}$$

Solution (42) indicates that at (ω_0, q_0) the right incidence $\boldsymbol{\varphi}^0$ penetrates into the space–time modulated medium exponentially decaying to vanish within a distance of order $\frac{1}{|\delta q_c|}$, and then is reflected into $\boldsymbol{\varphi}^1(\omega_1, q_1)$ propagating at q_1 opposite to q_0. This behavior is graphically illustrated as two band gaps at the locking pairs C, as shown in Fig. 3.

2. Numerical results and discussions

2.1. Prediction of dispersion curve

To validate our analytical modeling, a transient simulation is conducted using COMSOL Multiphysics to predict the dispersion curve in the modulated system. A 2-cycle broadband burst signal, centered at $\omega_c = \Omega$ and described as $A_0 \sin(\omega_c t)\left[1 - \cos(\omega_c t/2)\right]$ is used to generate Rayleigh waves propagating in different directions, as shown in Fig. 6(a). The low-reflecting boundaries are adopted in the ends of boundary to reduce reflection. On the surface, 600 oscillators are distributed uniformly with a spacing $l_s = \lambda_m/20$. Dispersion curve of Rayleigh wave propagation in the system with oscillators is numerically secured, which is also validated by analytical solution (see Appendix F). After that, the space–time modulation is applied to 600 oscillators and numerical simulation is then conducted to obtain time-domain signals of the Rayleigh wave at different locations. The 2D Fourier transform in space and in time is adopted on the obtained signals to retrieve the dispersion curve with non-zero modulation for both directions. The results

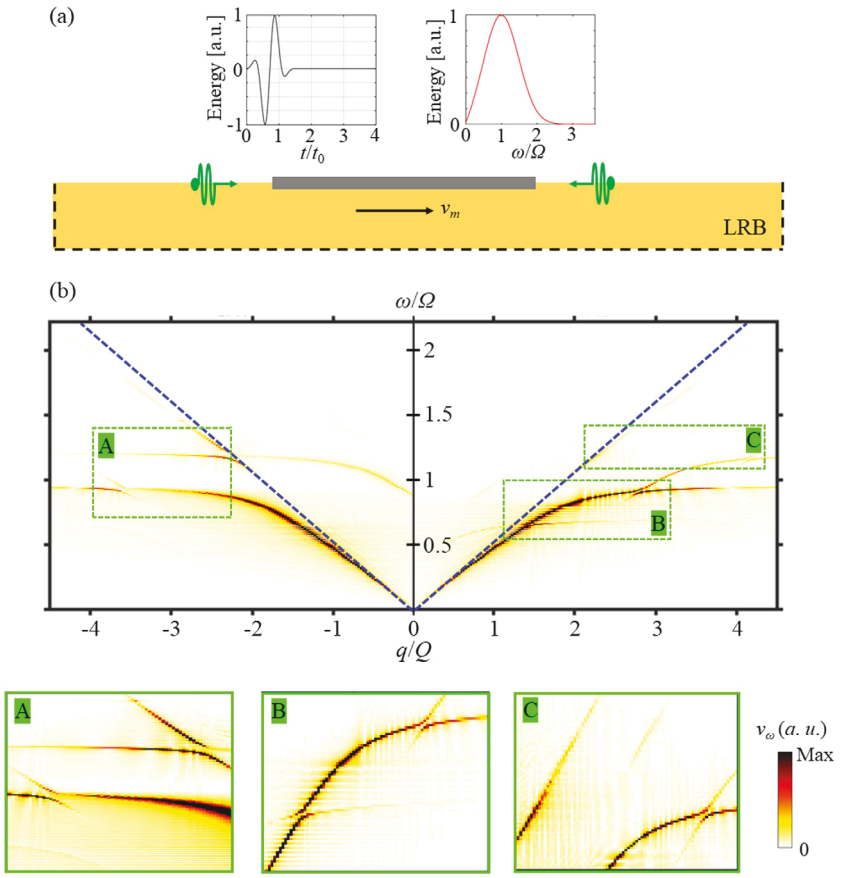

Fig. 6. (a) Schematic illustration of the numerical model used to retrieve the dispersion curve. The top panel gives the time- and frequency-domain spectra of the excitation. The bottom panel shows the numerical model, with a space–time modulation (STM) area highlighted in gray and composed of 600 oscillators. The black dashed arrow indicates the modulation direction. Two sources carrying the above excitation are placed, as highlighted in green. The low-reflecting boundaries (LRBs) are applied to minimize the effects of the undesired reflected waves. (b) The recovered dispersion curve is numerically obtained through a 2D Fourier transform. The blue dashed lines correspond to the dispersion curve of shear bulk waves. In particular, the green windows highlight the two pairs (A) and (B) and the coupling between the first-order and second-order harmonics (C). The color maps of the insets are adjusted accordingly for better visualization of the details of dispersion relation.

are shown in Fig. 6(b) and great agreement with the analytical prediction is illustrated in Fig. 3(d). In the figure, two non-reciprocal veering pairs A and B discussed in the analytical section can be directly visualized. However, the locking pair C at lower frequencies is hardly seen in Fig. 6(b) due to its extremely narrow band gap for the given modulation parameters. Anyway, the non-reciprocal scattering is numerically witnessed here in the vicinity of the two veering pairs on the recovered dispersion curves. Scattering of elsewhere on the dispersion curve of fundamental harmonic will be reciprocal. Aside from the couplings between the fundamental and first-order harmonics, we can also observe the couplings between other higher-order harmonics. In particular, one of them is highlighted in Fig. 6(b) by the green window (C), which reveals the coupled mode $\boldsymbol{\varphi}^1 \cap \boldsymbol{\varphi}^2$. This has not been discussed in detail in the analytical section since the strengths of the higher-order couplings are relatively weak compared to the ones of lower-order couplings, as can be seen in Fig. 6(b).

2.2. Non-reciprocal transmission

Numerical simulation is also conducted to confirm the non-reciprocal propagation of the Rayleigh wave, as shown in Fig. 7(a). We first test the non-reciprocity at the veering pair B $(0.668\ \Omega, 1.469Q)$, which corresponds to the case of the right-going Rayleigh wave by placing a modulation area comprising of 1000 unit cells between two free surfaces. The excitation used here is once again the tone burst signal, but with a much narrower linewidth (50 cycle) and a center frequency at $0.668\ \Omega$. The source, highlighted as the green point in Fig. 7, here consists of only a single point load which is embedded in the space–time modulation area. The excited Rayleigh wave propagates along two opposite directions; see Fig. 7(a). The time-domain signals, collected at the two highlighted points, are shown in Fig. 7(b) for both directions of Rayleigh wave propagation. For the right-going incidence, i.e. along the modulation direction, the time-domain response (red in Fig. 7(b)) is greatly distorted and delayed due to the coexistence of modes $\boldsymbol{\varphi}^0$, $\boldsymbol{\varphi}^1$ and even $\boldsymbol{\varphi}^2$ with difference group velocities. While for the left-going incidence (blue dashed in Fig. 7(b)), the time-domain signal

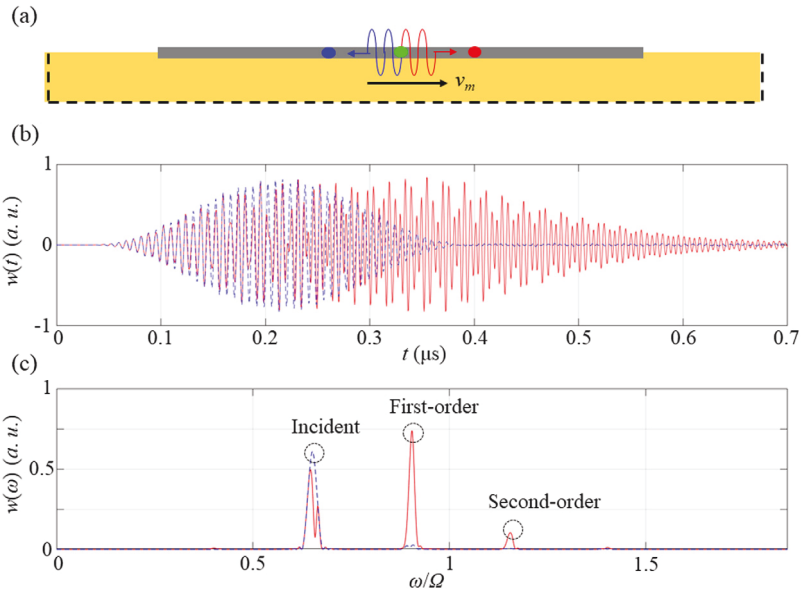

Fig. 7. Schematic illustrations of the simulation models. Unlike the previous case of retrieving the dispersion diagram, there are in total 1000 spring–mass oscillators involved, and a point load, embedded in the center of the space–time modulation area, is assigned to serve as the source. Two points (red and blue) separating equally to the source are designated to collect the time-domain response. The arrow denotes the direction of modulation. In this way, the red point corresponds to the Rayleigh wave propagation along the direction of modulation while the blue one indicates the opposite scenario. (b) presents the time-domain signals collected at the two points indicating different directions of incidence. The corresponding frequency-domain spectra (c) are derived through Fourier transform. The nearly total conversion of pair B takes place at the spectral position highlighted by the circles. (For interpretation of the references to colour in this figure legend, the reader is referred to the web version of this article.)

resembles the excitation, indicating that the modulation barely functions for this direction. The corresponding frequency spectra are illustrated in Fig. 7(c) through Fourier transformation of the time-domain data. Comparison between the illustrated results prove the non-reciprocity at the veering pair B. The right-going Rayleigh wave at $\boldsymbol{\varphi}^0(0.668\ \Omega, 1.469Q)$ nearly undergoes a total conversion into the first-order harmonic $\boldsymbol{\varphi}^1(0.668\ \Omega + \omega_m, 1.469Q + q_m)$ and even the second-order harmonic $\boldsymbol{\varphi}^1(0.668\ \Omega + 2\omega_m, 1.469Q + 2q_m)$, as has been denoted by the black circles in Fig. 7(c). On the contrary, the left-going Rayleigh wave at $\boldsymbol{\varphi}^0$ does not experience any conversion, demonstrating non-reciprocal propagation of the Rayleigh wave in our proposed system. Fig. 8(a) and (b) show the harmonic frequency spectra against the oscillator positions for the two opposite propagation directions. The spectra were produced through Fourier transform upon the time-domain data of displacement w collected at all the spring–mass oscillators. They reveal the harmonic conversion process while the Rayleigh waves propagate in the two opposite directions. In Fig. 8(a), since the propagation direction is identical to the modulation speed v_m, the incidence excites both the first- and second-order harmonics (see Fig. 7). During the propagation within the modulated area, the intensity of the incident fundamental harmonic component reaches the local maximum when the first-order and second-order harmonic components reach their local minimums, and vice versa. While for the left-going wave, no such conversion occurs, and the intensity of the incident harmonic component remains unchanged when the wave propagates in the left direction [see Fig. 8(b)]. In Figs. 8(c) and (d), we plot the time-frequency-amplitude maps for the two receiver stations indicated as blue and red points in Fig. 7. Since there always exists a trade-off between the frequency and time resolutions, here we set the frequency resolution as 0.0233 Ω, corresponding to a time resolution of 0.1243 μs. Three different colors are used to highlight the analytically predicted frequencies of the incident fundamental, excited first- and second-order harmonics. Fig. 8(c) shows the results collected at the red point (identical position of the red point in Fig. 7) for the right-going wave. The incident harmonic is converted into the first-order and second-order harmonics soon after the incidence reaches the red point. The first-order and second-order harmonic components last longer in time at this receiver station than the incident harmonic one does since the group velocities of the first-order and second-order harmonics are smaller than that of the incident harmonic (see Figs. 3 and 6). In addition, along the modulation direction, the incident harmonic component appears to be more durable in terms of time than that of the opposite case [see comparison between Fig. 8(c) and (d)]. This is simply because around the veering pairs $(\omega_{0\cap 1}, q_{0\cap 1})$ corrected by Eq. (36), the dispersion curve gives smaller group velocities when compared to the uncoupled area $(\omega_{0\cap 1}, -q_{0\cap 1})$ (see Figs. 3 and 6). As for the left-going Rayleigh wave, nearly no conversion between the incident and the higher order harmonics can be visualized [see Fig. 8(d)]. Note that the results in Fig. 8(c) and (d) can clearly illustrate the non-reciprocal harmonic conversion, even though the time resolution is not considered high owing to the compromise we have made between the transient simulation efficiency and the simulation time span (currently 0.85 μs). To better the quality of the time-frequency-amplitude maps, one can increase the simulation time span while preserving the current simulation sampling frequency (currently 8 GHz).

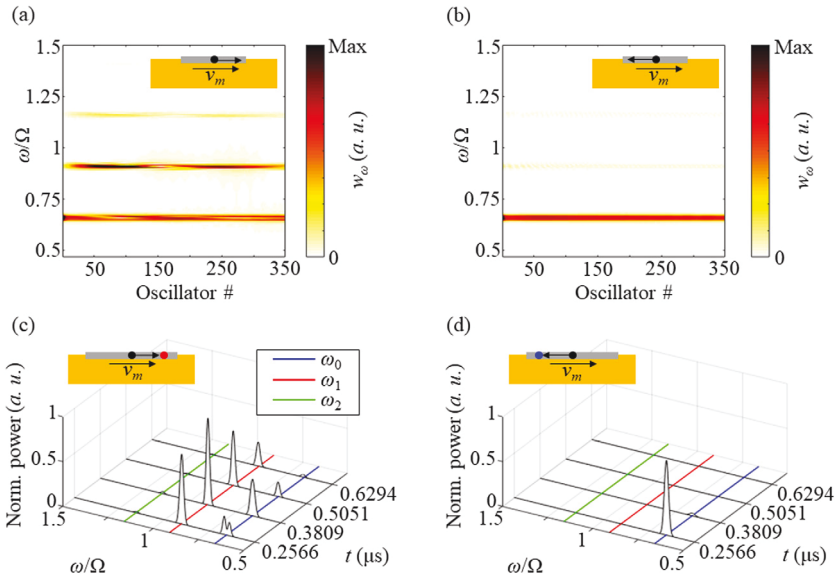

Fig. 8. Illustration of the harmonic conversion process. (a) and (b) Evolution of the harmonic spectra of the Rayleigh waves propagating against the oscillator position along the two opposite directions. (c) and (d) Time-frequency-amplitude maps for the two receiver stations in Fig. 7. (c) corresponds to the right-going wave collected at the red point, while (d) corresponds to the left-going wave collected at the blue point. In (c) and (d), the blue, red and green lines represent the frequencies of the incident fundamental, excited first-order and second-order harmonics, respectively. The frequency resolution is taken as 0.0233 Ω, which consequently leads to a time resolution of 0.1243 μs. (For interpretation of the references to colour in this figure legend, the reader is referred to the web version of this article.)

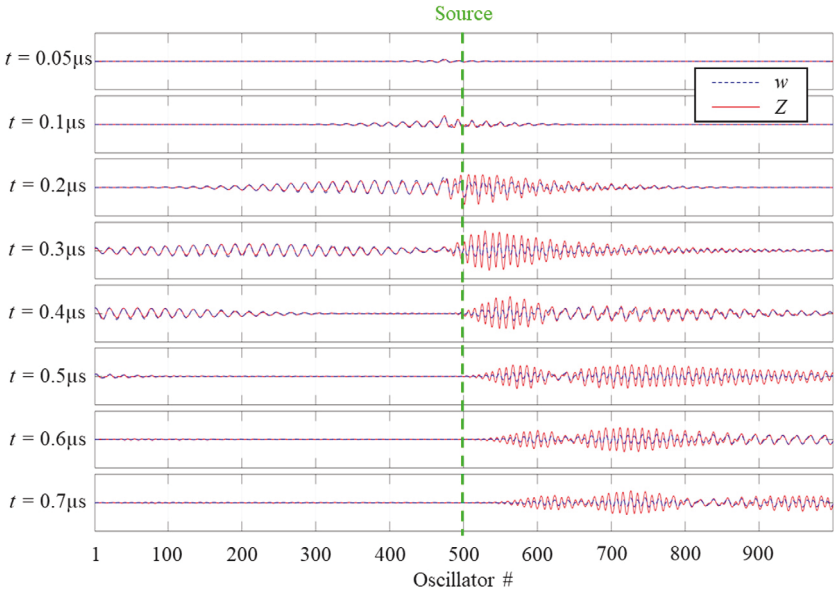

Fig. 9. Mode conversion of pair B. The displacements of oscillator masses Z (red solid) and the displacement $2w$ (blue dashed) are plotted against the oscillator position at various time instants. For clear observation, the vertical displacement w has been magnified by 2. The green dashed line represents the position of the source.

2.3. One-way mode conversion

Mode conversion of Rayleigh waves can be realized in the proposed system. The spectral relocation of the energy of the veering pair B shown in Fig. 7(c) refers to an acoustic–acoustic conversion, as can be concluded from Fig. 3(b) and (d). It indicates that the incidence starts from in-phase oscillations between the displacement of oscillator mass Z and the vertical displacement of the surface w undergoes a transition between higher-order harmonics, and still remains in-phase. As can be seen in Fig. 9, at t = 0.05

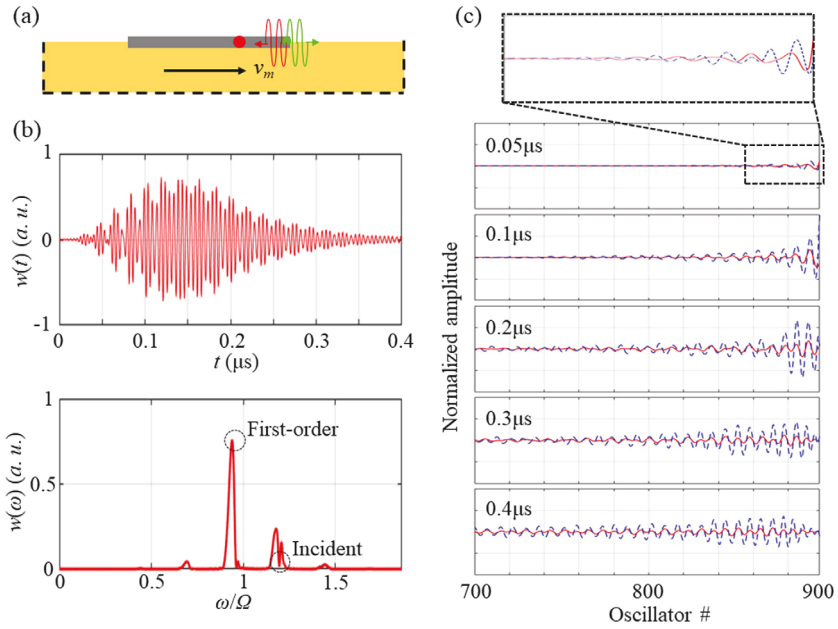

Fig. 10. (a) The center frequency of the tone-burst is selected so as to match pair A. Other settings are identical to those in Fig. 7 except only 900 oscillators are included and the source is still positioned inside the modulation area but close to the right end of the modulation area. (b) The time-domain and the corresponding frequency-domain spectrum are presented, showing the generation of higher-order harmonics. (c) Similar to Fig. 9, the time-domain signals for Z (blue dashed) and $2w$ (red solid) are shown in functions of oscillator position at different time instants. The inset provides a magnified view of the initial state of the combined spring–mass semi-infinite system.

μs, the system starts from in-phase oscillations between Z (blue dashed) and $2w$ (red solid). As the Rayleigh wave propagates along the modulation direction (right half of Fig. 9), it undergoes a mode conversion from $\boldsymbol{\varphi}^0$, with longer wavelength, to $\boldsymbol{\varphi}^1$, with shorter wavelength. The oscillator mass displacements Z are obviously amplified after $t = 0.2$ μs due to the fact that the generated first-order harmonics $\boldsymbol{\varphi}^1$ locates quite close to the resonance frequency Ω; see Fig. 3. Moreover, $\boldsymbol{\varphi}^1$ propagates slower than $\boldsymbol{\varphi}^0$ does, since they differs in terms of group velocity; see Fig. 3. Compared to the mode conversion case, the trivial scenario with the direction of incidence opposite to the modulation direction exhibits neither mode conversion nor amplified displacement Z, as can be seen from the left half of Fig. 9. The oscillation between Z and w remains in-phase, once again indicating the acoustic branch. Interestingly, slow wave phenomenon for the incidence $\boldsymbol{\varphi}^0$ can also be observed as can be seen from the comparison between these two cases. The propagation speeds for two opposite directions are different. Most importantly, the mode conversion in our proposed system is not restricted to acoustic–acoustic and the conversion between acoustic and optical modes can be achieved by choosing appropriate modulation parameters (ω_m, λ_m). In Fig. 10, we send in a tone-burst signal centered at 1.18 Ω at the green point, which corresponds to the selection of the veering pair A (Fig. 3(a)). Similarly to the case of pair B, nearly total conversion can be observed from $\boldsymbol{\varphi}^0$ at 1.17 Ω to $\boldsymbol{\varphi}^1$ at 1.18 Ω − ω_m, as illustrated in Fig. 10(b). To reveal the optical–acoustic conversion of this pair, we then plot in Fig. 10(c) the transient signal against the oscillator position as we have already done for pair B in Fig. 9. Unlike pair B, the system operating at pair A initiates from out-of-phase oscillations of Z and w at the instant $t = 0.05$ μs, corresponding to the optical mode; see the highlighted inset of Fig. 10(c) for an amplified view. While the Rayleigh wave propagates along the correct direction, namely, opposite to the modulation direction, it undergoes a conversion from the optical mode to the acoustic one and the relative phase difference between Z and w gradually vanishes, suggesting that the system operates now at the acoustic mode. Also, at the output frequency 1.18 Ω − ω_m close to the resonant frequency Ω, the strength of Z experiences a great amplification.

3. Conclusion

In summary, we theoretically introduce a strategy to realize the non-reciprocal propagation of Rayleigh waves and the associated one-way mode conversion, with the help of space–time modulated spring–mass oscillators distributed on the surface of the hosting medium. In the proposed system, the spring constant is modulated temporarily and spatially at the same time in a wave-like fashion. The resulting “pump wave” breaks the time-reversal symmetry, and hence gives birth to the non-reciprocal phenomena. The interactions between this “pump wave” and the traveling Rayleigh wave deliver a remarkable consequence that the group velocities in the vicinity of the interactions require to be corrected accordingly. Analytical and numerical approaches well recover the perturbed dispersion diagram in the presence of the space–time modulation. More importantly, three non-reciprocal pairs, enabling non-reciprocal propagations of Rayleigh waves, are revealed by solving the coupling of harmonics around the interaction points. One of them exhibits the one-way mode conversion between the acoustic and the optical modes. Further, tunability has been investigated as well to provide information and guidance for the potential experimental implementations in the future.

CRediT authorship contribution statement

Qian Wu: Conceptualization, Formal analysis and modeling, Methodology, Writing - review & editing. **Hui Chen:** Formal analysis, Methodology. **Hussein Nassar:** Formal analysis, Methodology. **Guoliang Huang:** Conceptualization, Validation, Supervision, Funding acquisition, Writing - review & editing.

Declaration of competing interest

The authors declare that they have no known competing financial interests or personal relationships that could have appeared to influence the work reported in this paper.

Acknowledgment

This work is supported by NSF EFRI under award No. 1641078, the NSF CMMI under Award No. 1930873 with Program Manager Dr. Nakhiah Goulbourne, and the Army Research Office under Grant No. W911NF-18-1-0031 with Program Manager Dr. Daniel P Cole.

Appendix A. Derivation of characteristic equation of Rayleigh wave to the leading order

Due the similarity between Eqs. (11) and (12), we mainly focus on the derivation related to Eq. (11). By solving Eq. (11) for $D_1^j(z)$ and considering Rayleigh waves decaying towards $+z$-direction, the leading-order terms of the jth-order harmonic component of expression (9) reads

$$\Phi^j = A_1 e^{-q_j p_j z} e^{ij\xi} e^{i(\tilde{q}x-\tilde{\omega}t)} \tag{43}$$

with $p_j = \sqrt{1-\omega_j^2/c_L^2 q_j^2}$. Similarly, one can obtain the leading-order shear potential function as

$$\Psi^j = B_1 e^{-q_j s_j z} e^{ij\xi} e^{i(\tilde{q}x-\tilde{\omega}t)} \tag{44}$$

with $s_j = \sqrt{1-\omega_j^2/c_T^2 q_j^2}$. In above equations, A_1 and B_1 are arbitrary wave amplitudes. Therefore, the leading-order terms of displacements u and w of the jth-order harmonic can be obtained as

$$u^j = \partial_x \Phi^j + \partial_z \Psi^j = q_j (iA_1 e^{-q_j p_j z} - s_j B_1 e^{-q_j s_j z}) e^{ij\xi} e^{i(\tilde{q}x-\tilde{\omega}t)} \tag{45}$$

$$w^j = \partial_z \Phi^j - \partial_x \Psi^j = -q_j (p_j A_1 e^{-q_j p_j z} + iB_1 e^{-q_j s_j z}) e^{ij\xi} e^{i(\tilde{q}x-\tilde{\omega}t)} \tag{46}$$

and the leading-order terms of the two stress components can be written as

$$\sigma_{zz}^j = \mu\ q_j^2 (r_j A_1 e^{-q_j p_j z} + 2is_j B_1 e^{-q_j s_j z})\ e^{ij\xi} e^{i(\tilde{q}x-\tilde{\omega}t)} \tag{47}$$

$$\sigma_{xz}^j = \mu\ q_j^2 (-2ip_j A_1 e^{-q_j p_j z} + r_j B_1 e^{-q_j s_j z})\ e^{ij\xi} e^{i(\tilde{q}x-\tilde{\omega}t)} \tag{48}$$

where μ is the shear modulus and $r_j = 2 - \omega_j^2/c_T^2 q_j^2$. On the other hand, the equation of motion of surface oscillators is written as

$$m\partial_t^2 Z^j + K_m \left(Z^j - w_{z=0}^j \right) = 0 \tag{49}$$

where Z^j is the jth-order harmonic component of the mass displacement up to the leading-order correction. Assuming a traveling wave solution reading $Z = \sum_{j\in\mathbb{Z}} Z_0^j e^{ij\xi} e^{i(\tilde{q}x-\tilde{\omega}t)}$ for the oscillator mass motion and keeping only the leading-order terms, Eq. (49) becomes then

$$Z^j = \frac{\Omega^2 w_{z=0}^j}{\Omega^2 - \omega_j^2} \tag{50}$$

where $\Omega = \sqrt{K/m}$ represents the resonant frequency of the unperturbed oscillators. The exerted stress by the oscillators on the surface reads

$$\sigma_{zz}^{osc} = \frac{K_2 (Z_0^j - w_0^j)}{A} = \frac{K\omega_j^2 w_{z=0}^j}{A\left(\Omega^2 - \omega_j^2\right)} \tag{51}$$

with A denoting the occupied area of each oscillator. Applying the boundary conditions $\sigma_{zz,z=0}^j = -\sigma_{zz}^{osc}$ and $\sigma_{xz,z=0}^j = 0$ and eliminating the two arbitrary wave amplitudes, we obtain the characteristic equation of leading-order correction which describes the Rayleigh wave dispersion in the presence of space–time modulated oscillators (see Eq. (14) in the main text).

Appendix B. Derivation of orthogonality condition

Following the effective body forces given in the main text and considering the fact that the first-order correction terms are all periodic with respect to ξ, we take average on the forced governing equations to eliminate the propagating effect along the x-direction as

$$\begin{bmatrix} -q_0^2(2\mu+\lambda)+\mu\partial_z^2 & iq_0(\mu+\lambda)\partial_z \\ iq_0(\mu+\lambda)\partial_z & (2\mu+\lambda)\partial_z^2-q_0^2\mu \end{bmatrix}\delta\boldsymbol{\varphi}+\boldsymbol{F}=-\omega_0^2\rho\delta\boldsymbol{\varphi} \tag{52}$$

$$-K\left(\langle\delta Z\rangle-\langle\delta w_{z=0}\rangle\right)+\langle G\rangle=-\omega_0^2 m\langle\delta Z\rangle \tag{53}$$

$$\left(iq_0\mu\langle\delta w\rangle+\mu\partial_z\langle\delta u\rangle\right)_{z=0}=\langle H\rangle \tag{54}$$

$$\left[iq_0\lambda\langle\delta u\rangle+(2\mu+\lambda)\partial_z\langle\delta w\rangle\right]_{z=0}=-K/A\left(\langle\delta Z\rangle-\langle\delta w_{z=0}\rangle\right)+\langle I\rangle \tag{55}$$

where the averaging operator takes the form of $\langle\rangle\equiv 1/2\pi\int_0^{2\pi}$. By projecting the governing equation (52) onto the complex conjugate mode shape $\boldsymbol{\varphi}^*$ and integrating over the semi-infinite space along the $+z$-direction, we have

$$\begin{aligned} &-iq_0\lambda\left(u^{ast}\langle\delta w\rangle\right)_{z=0}-\left[u^*\left(iq_0\mu\langle\delta w\rangle+\mu\partial_z\langle\delta u\rangle\right)\right]_{z=0}+\mu\left(\partial_z u^*\langle\delta u\rangle\right)_{z=0}\\ &-\left[u^*\left(iq_0\lambda\langle\delta u\rangle+(2\mu+\lambda)\partial_z\langle\delta w\rangle\right)\right]_{z=0}-iq_0\mu\left(w^*\langle\delta u\rangle\right)_{z=0}\\ &+(2\mu+\lambda)\left(\partial_z w^*\langle\delta w\rangle\right)_{z=0}+\int_0^\infty\boldsymbol{\varphi}^*\cdot\langle\boldsymbol{F}\rangle\,dz=0 \end{aligned} \tag{56}$$

The presence of the space–time modulation in this work makes the whole system a forced and non-Hermitian (non self-adjoint) system, which could be readily seen from Eq. (56) having been left multiplied by the complex conjugate eigenvector $\boldsymbol{\varphi}^*$ and right multiplied by $\delta\boldsymbol{\varphi}$ (being left multiplied by $\boldsymbol{\varphi}$ will simply lead to complex eigenvalues rather than the current negative, real ones). Following the notation in Mokhtari et al. (2019), this further implies the bi-orthogonality relation $\int_0^\infty\boldsymbol{\varphi}^*\boldsymbol{B}\delta\boldsymbol{\varphi}dz=0$, where the operator $\boldsymbol{B}$ is an identity matrix in this work. In addition, the continuous part of the forced system has non-zero modulation-induced effective body force $\boldsymbol{F}$. As has been mentioned in the main text, in order for this system to remain stable, the body force needs to do deliver zero work within the entire semi-infinite medium, i.e. $\int_0^\infty\boldsymbol{\varphi}^*\cdot\langle\boldsymbol{F}\rangle\,dz=0$ must hold, which returns equation (56) and corresponds to a continuous version of the discrete orthogonality condition presented in our recent paper (Nassar et al., 2017b). Based on the governing equation (53) and boundary conditions (54) and (55), and considering the complex conjugates of the leading-order stress boundary conditions and the governing equation of motion of oscillators, we further simplify Eq. (56) into

$$\begin{aligned} &\frac{m\omega_0^2}{A}\left(w^*_{z=0}\langle\delta Z\rangle-Z^*\langle\delta w_{z=0}\rangle\right)+w^*_{z=0}\left(\frac{\langle G\rangle}{A}-\langle I\rangle\right)\\ &-u^*_{z=0}\langle H\rangle+\int_0^\infty\boldsymbol{\varphi}^*\cdot\langle\boldsymbol{F}\rangle\,dz=0 \end{aligned} \tag{57}$$

Combining Eqs. (13), (53) and (57), we reach eventually the orthogonality condition (28) in the main text.

$$w^*_{z=0}\left(\frac{Q_0}{A}\langle G\rangle-\langle I\rangle\right)-u^*_{z=0}\langle H\rangle+\int_0^\infty\boldsymbol{\varphi}^*\cdot\langle\boldsymbol{F}\rangle\,dz=0 \tag{58}$$

Appendix C. Expressions of a_j and b_j

In the main context, the detailed expressions of a_j and b_j, $j\in\mathbb{Z}$, can be expressed as

$$\begin{aligned} a_j=&\,2(\mu+\lambda)q_j^2p_j\frac{(s_jp_j-1)(s_j-p_j)}{r_j(p_j+s_j)}-2q_j^2(2\mu+\lambda)\left(\frac{1}{2p_j}-\frac{4s_jp_j}{r_j(p_j+s_j)}+\frac{2s_jp_j^2}{r_j^2}\right)\\ &-2\mu q_j^2p_j^2\left(\frac{1}{2p_j}-\frac{4}{r_j(p_j+s_j)}+\frac{2}{r_j^2s_j}\right)-\mu q_j^2p_j\left(1-\frac{2}{r_j}\right)\left(1-2\frac{s_jp_j}{r_j}\right)\\ &+\lambda q_j^2p_j\left(1-\frac{2}{r_j}\right)\left(1-\frac{2s_jp_j}{r_j}\right)\\ b_j=&\,2q_j\rho\omega_j\left(\frac{1}{2p_j}-\frac{4s_jp_j}{r_j(p_j+s_j)}+\frac{2s_jp_j^2}{r_j^2}\right)+2q_j\,p_j^2\rho\omega_j\left(\frac{1}{2p_j}-\frac{4}{r_j(p_j+s_j)}+\frac{2}{r_j^2s_j}\right)\\ &-\frac{2m}{A}\omega_jq_jp_j\left(1-\frac{2}{r_j}\right)Q_jZ^j \end{aligned} \tag{59}$$

Appendix D. Derivation of the first-order correction on the dispersion curves of coupled modes

Similarly to the uncoupled scenario, we take average on the complete effective body forces for the coupled scenario in Eq. (33). In this case, the first-order harmonic $\boldsymbol{\varphi}^1$ is eliminated. The averaged effective body forces are the same as Eq. (29), except for the averaged body forces $\langle G\rangle^0$ and $\langle I\rangle^0$ taking different forms

$$\langle G\rangle^0=-V_1\left\langle\delta Ke^{i\xi}\right\rangle\left(Z^1-w^1_{z=0}\right)+2m\omega_0\delta\omega V_0Z^0 \tag{60}$$

$$\langle I\rangle^0 = V_1\frac{\left\langle \delta K(\xi)\, e^{i\xi}\right\rangle}{A}\left(Z^1 - w^1_{z=0}\right) - i\lambda\delta q V_0 u^0_{z=0} \tag{61}$$

Multiplying the effective body forces (33) by $e^{-i\xi}$ and operating average simply gets rid of the fundamental harmonic $\boldsymbol{\varphi}^0$ and return the effective body forces of the first-order harmonic $\boldsymbol{\varphi}^1$.

$$\langle \boldsymbol{F}\rangle^1 = \begin{bmatrix} V_1\left[-2q_1\delta q(2\mu+\lambda) + 2\rho\omega_1\delta\omega\right]u^1 + i(\mu+\lambda)\delta q\partial_z V_1 w^1 \\ V_1\left[-2\mu q_1\delta q + 2\rho\omega_1\delta\omega\right]w^1 + i(\mu+\lambda)\delta q\partial_z V_1 u^1 \end{bmatrix} \tag{62}$$

$$\langle G\rangle^1 = -V_0\left\langle \delta K e^{-i\xi}\right\rangle\left(Z^0 - w^0_{z=0}\right) + 2m\omega_1\delta\omega V_1 Z^1 \tag{63}$$

$$\langle H\rangle^1 = -i\mu\delta q V_1 w^1_{z=0} \tag{64}$$

$$\langle I\rangle^1 = V_0\frac{\left\langle \delta K(\xi)\, e^{-i\xi}\right\rangle}{A}\left(Z^0 - w^0_{z=0}\right) - i\lambda\delta q V_1 u^1_{z=0} \tag{65}$$

As can be seen from the expressions (60), (61), (63) and (65), the non-zero space–time modulation $\delta K(\xi)$ comes into play and gives rise to the interaction between modes $\boldsymbol{\varphi}^1$ and $\boldsymbol{\varphi}^0$. Substituting Eqs. (29), (60), (61) and (62)–(65) into the orthogonality condition (28) yields Eq. (34) in the main text.

$$\begin{bmatrix} \mathcal{E}_{11} & \mathcal{E}_{12} \\ \mathcal{E}_{21} & \mathcal{E}_{22}\end{bmatrix}\begin{bmatrix} V_0 \\ V_1\end{bmatrix} = \mathcal{E}\begin{bmatrix} V_0 \\ V_1\end{bmatrix} = 0 \tag{66}$$

where

$$\begin{aligned} \mathcal{E}_{11} &= a_0\delta q + b_0\delta\omega \\ \mathcal{E}_{12} &= q_0 p_0\frac{\delta K}{A}(1-\frac{2}{r_0})\left(Z^1 + q_1 p_1(1-\frac{2}{r_1})\right)(Q_0+1) \\ \mathcal{E}_{21} &= q_1 p_1\frac{\delta K}{A}(1-\frac{2}{r_1})\left(Z^0 + q_0 p_0(1-\frac{2}{r_0})\right)(Q_1+1) \\ \mathcal{E}_{22} &= a_1\delta q + b_1\delta\omega \end{aligned} \tag{67}$$

and $\left\langle \delta K e^{i\xi}\right\rangle = \left\langle \delta K e^{-i\xi}\right\rangle = \delta K$.

Appendix E. Details of deriving the conversion parameters of veering pairs

In this appendix, the derivation highly resembles that introduced in Nassar et al. (2017b). For the veering pairs discussed in the main text, we repeat the group velocities for the uncoupled harmonics:

$$v_g^0 = -\frac{a_0}{b_0},\quad v_g^1 = -\frac{a_1}{b_1} \tag{68}$$

Substituting expression (68) into Eq. (36) and rearranging the resulting equation yields

$$\delta q_\pm = \frac{\delta\omega}{2}\left(\frac{1}{v_g^0}+\frac{1}{v_g^1}\right) \pm \sqrt{\left[\frac{\delta\omega}{2}\left(\frac{1}{v_g^0}-\frac{1}{v_g^1}\right)\right]^2 + \frac{\mathcal{E}_{12}\mathcal{E}_{21}}{b_0 b_1 v_g^0 v_g^1}} = \pm\delta q_a + \delta q_b \tag{69}$$

By assuming a conversion coefficient $C = \frac{V_1}{V_0}$, we have

$$C_\pm = \left(\delta q_\pm - \frac{\delta\omega}{v_g^0}\right)\frac{b_0 v_g^0}{\mathcal{E}_{12}} = \left(\left(\frac{1}{v_g^1}-\frac{1}{v_g^0}\right)\delta\omega \pm \left(\delta q_+ - \delta q_-\right)\right)\frac{b_0 v_g^0}{2\mathcal{E}_{12}} = \pm C_a + C_b \tag{70}$$

When the excitation frequency $\omega_0 + \delta\omega$ is close to the intersection frequency of the coupled mode ω_0, based on Eqs. (69) and (70), the wave solution is a superposition of the two possible wave components

$$\begin{aligned} \boldsymbol{\varphi}(x,t) &= \left(V_0\boldsymbol{\varphi}^0 e^{i(q_0 x-\omega_0 t)} + V_1\boldsymbol{\varphi}^1 e^{i(q_1 x-\omega_1 t)}\right)e^{i(\delta q x-\delta\omega t)} \\ &= \left[V_{0+}e^{i\delta q_a x}\left(\boldsymbol{\varphi}^0 e^{i(q_0 x-\omega_0 t)} + \left(C_a+C_b\right)\boldsymbol{\varphi}^1 e^{i(q_1 x-\omega_1 t)}\right)\right]e^{i(\delta q_b x-\delta\omega t)} \\ &+ \left[V_{0-}e^{-i\delta q_a x}\left(\boldsymbol{\varphi}^0 e^{i(q_0 x-\omega_0 t)} - \left(C_a-C_b\right)\boldsymbol{\varphi}^1 e^{i(q_1 x-\omega_1 t)}\right)\right]e^{i(\delta q_b x-\delta\omega t)} \end{aligned} \tag{71}$$

Without loss of generality, let us assume $x = 0$ is where the Rayleigh wave enters the modulated area. In order for $\boldsymbol{\varphi}^0$ to be the only existing one at $x = 0$, we take $V_{0\pm} = \left(C_a \mp C_b\right)V_0$. In this way, the previous solution (71) becomes

$$\begin{aligned} \boldsymbol{\varphi}(x,t) = 2V_0[&C_a\cos\left(\delta q_a x\right)\boldsymbol{\varphi}^0 e^{i(q_0 x-\omega_0 t)} - iC_b\sin\left(\delta q_a x\right)\boldsymbol{\varphi}^0 e^{i(q_0 x-\omega_0 t)} \\ &+ i\left(C_a^2 - C_b^2\right)\sin\left(\delta q_a x\right)\boldsymbol{\varphi}^1 e^{i(q_1 x-\omega_1 t)}]e^{i(\delta q_b x-\delta\omega t)} \end{aligned} \tag{72}$$

As x increases, the amplitude of $\boldsymbol{\varphi}^0$ decreases due to the fact that $|C_a| \geq |C_b|$ as long as the space–time modulation is turned on. Meanwhile, the amplitude of $\boldsymbol{\varphi}^1$ starts to increase. At $x = d = \pi/\left(2\delta q_a\right)$, $\boldsymbol{\varphi}^0$ reaches its minimum while $\boldsymbol{\varphi}^1$ reaches the maximum.

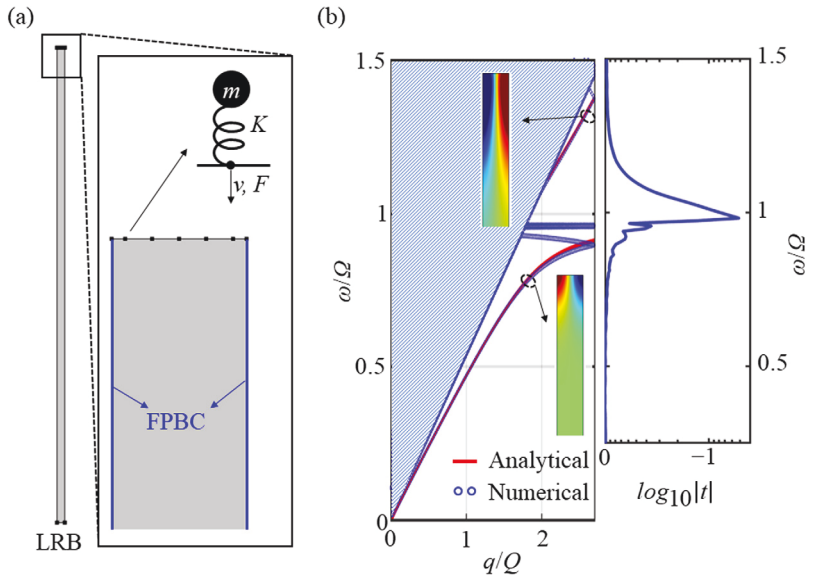

Fig. 11. (a) Schematic illustration of the supercell which represents a horizontally infinite semi-infinite medium decorated by non-modulated ($\delta K = 0$) spring–mass oscillators on the top surface. The discrete points represent the spring–mass oscillators. The top surface is set free while the bottom one is set with low-reflecting boundary condition (LRB). The two highlighted in blue are Floquet periodic boundary conditions (FPBCs). The z-directional displacement and the exerted force by the oscillators are recorded and extracted at the contact point. (b) The bulk band structure obtained from the modal analysis of the supercell is shown in the left panel. The numerical and analytical results agree well, except for the zone-folding curves. The mode shapes of the two highlighted branches are also extracted. The corresponding transmission coefficient, shows band gap for the Rayleigh wave around the resonance frequency, which exhibits great agreement with the supercell analysis.

Typically, the total conversion from $\boldsymbol{\varphi}^0$ to $\boldsymbol{\varphi}^1$ can be expected when $C_b = 0$, namely, $\delta\omega = 0$. In this case, we have the following expressions in the main text.

$$\delta q_{\pm} = \pm\sqrt{\frac{\mathcal{E}_{12}\mathcal{E}_{21}}{b_0 b_1 v_g^0 v_g^1}}, \quad C_{\pm} = \pm\frac{b_0 v_g^0}{\mathcal{E}_{12}}\sqrt{\frac{\mathcal{E}_{12}\mathcal{E}_{21}}{b_0 b_1 v_g^0 v_g^1}} \tag{73}$$

Appendix F. Numerical validation of the unmodulated model

To verify the theoretical part, we conduct numerical simulations using the commercial software COMSOL Multiphysics. In the theoretical section, we assume a continuous span of spring–mass oscillators whose spring constants are space–time modulated in a wave-like fashion. However, in real cases the distribution of oscillators cannot be continuous. In order to effectively model the continuous section, we construct discrete spring–mass oscillators separated by spacing l_s, as shown in Fig. 1, with the help of lumped mechanical system module, as shown in Fig. 11(a). At first, we start with unmodulated spring–mass oscillators to validate the simulation model. The parameters used here are identical to those used in the theoretical section (Fig. 1). As shown in Fig. 11(a), the numerically modeled supercell is shown with its top surface decorated by five non-modulated spring–mass oscillators ($\delta K = 0$). The spacing is chosen as $l_s = \lambda_m/20$. Since the chosen spacing is much smaller than the operating wavelength, according to the long wavelength assumption, the discrete oscillators can be equivalently treated as a continuous spring–mass layer at the surface. The low-reflecting boundary (LRB) condition is applied on the bottom boundary of the supercell for diminishing the undesired reflection of bulk waves from the bottom. The supercell is bounded horizontally by two vertical Floquet periodic boundaries highlighted in blue. In this way, the supercell well represents a horizontally infinite system. Discrete points are distributed on the top surface, corresponding to the spring–mass oscillators. The displacements w at the bottom ends of springs are extracted at the points on the top surface. By contrast, the forces F exerted by the oscillators on the top surface is calculated at the bottom ends of springs and then is applied on the discrete points. The modal analysis gives the calculated bulk band structure shown in the left panel of Fig. 11(b). The analytical and numerical obtained upper and lower branches are in good agreement. The existence of additional numerically obtained bands, which do not appear in the analytical section, is due to the zone folding since the supercell corresponds to a reducible lattice cell. The mode shapes for the upper (optical) and lower (acoustic) branches are also shown in the insets. They are out-of-phase due to the fact that the band gap is generated by the local resonance. To further verify the model, we construct an array of 600 non-modulated oscillators. Frequency-domain simulation produces the transmission coefficient which is shown in the right panel of Fig. 11(b). A band gap for the Rayleigh wave can be visualized, which agrees well with the modal analysis results. This further proves the validity of our simulation models.

References

Artru, J., Farges, T., Lognonné, P., 2004. Acoustic waves generated from seismic surface waves: propagation properties determined from doppler sounding observations and normal-mode modelling. Geophys. J. Int. 158 (3), 1067–1077.

Ash, B.J., Worsfold, S.R., Vukusic, P., Nash, G.R., 2017. A highly attenuating and frequency tailorable annular hole phononic crystal for surface acoustic waves. Nature Commun. 8 (1), 174.

Aubert, T., Elmazria, O., Assouar, B., Bouvot, L., Oudich, M., 2010. Surface acoustic wave devices based on aln/sapphire structure for high temperature applications. Appl. Phys. Lett. 96 (20), 203503.

Badreddine Assouar, M., Oudich, M., 2011. Dispersion curves of surface acoustic waves in a two-dimensional phononic crystal. Appl. Phys. Lett. 99 (12), 123505.

Benchabane, S., Salut, R., Gaiffe, O., Soumann, V., Addouche, M., Laude, V., Khelif, A., 2017. Surface-wave coupling to single phononic subwavelength resonators. Phys. Rev. A 8 (3), 034016.

Boechler, N., Eliason, J.K., Kumar, A., Maznev, A.A., Nelson, K.A., Fang, N., 2013. Interaction of a contact resonance of microspheres with surface acoustic waves. Phys. Rev. Lett. 111 (3), 036103.

Casadei, F., Delpero, T., Bergamini, A., Ermanni, P., Ruzzene, M., 2012. Piezoelectric resonator arrays for tunable acoustic waveguides and metamaterials. J. Appl. Phys. 112 (6), 064902.

Cassedy, E.S., 1967. Dispersion relations in time-space periodic media part ii—Unstable interactions. Proc. IEEE 55 (7), 1154–1168.

Cassedy, E., Oliner, A., 1963. Dispersion relations in time-space periodic media: Part i—Stable interactions. Proc. IEEE 51 (10), 1342–1359.

Chen, Y.Y., Huang, G.L., Sun, C.T., 2014. Band gap control in an active elastic metamaterial with negative capacitance piezoelectric shunting. J. Vib. Acoust. 136 (6), 1–8.

Chen, Y., Li, X., Nassar, H., Norris, A.N., Daraio, C., Huang, G., 2019. Nonreciprocal wave propagation in a continuum-based metamaterial with space-time modulated resonators. Phys. Rev. A 11 (6), 064052.

Colombi, A., Roux, P., Guenneau, S., Gueguen, P., Craster, R.V., 2016. Forests as a natural seismic metamaterial: Rayleigh wave bandgaps induced by local resonances. Sci. Rep. 6 (1), 19238.

Colquitt, D., Colombi, A., Craster, R., Roux, P., Guenneau, S., 2017. Seismic metasurfaces: Sub-wavelength resonators and Rayleigh wave interaction. J. Mech. Phys. Solids 99, 379–393.

Delsing, P., Cleland, A.N., Schuetz, M.J., Knörzer, J., Giedke, G., Cirac, J.I., Srinivasan, K., Wu, M., Balram, K.C., Bäuerle, C., et al., 2019. The 2019 surface acoustic waves roadmap. J. Phys. D: Appl. Phys. 52 (35), 353001.

Devkota, J., Ohodnicki, P., Greve, D., 2017. SAW sensors for chemical vapors and gases. Sensors 17 (4), 801.

Fleury, R., Sounas, D.L., Sieck, C.F., Haberman, M.R., Alù, A., 2014. Acoustic circulator. Science 343, 516–519.

Kadota, M., Ito, S., Ito, Y., Hada, T., Okaguchi, K., 2011. Magnetic sensor based on surface acoustic wave resonators. Japan. J. Appl. Phys. 50 (7), 07HD07.

Kadota, M., Nakao, T., Taniguchi, N., Takata, E., Mimura, M., Nishiyama, K., Hada, T., Komura, T., 2005. Surface acoustic wave duplexer for US personal communication services with good temperature characteristics. Japan. J. Appl. Phys. 44 (6B), 4527–4531.

Khelif, A., Achaoui, Y., Benchabane, S., Laude, V., Aoubiza, B., 2010. Locally resonant surface acoustic wave band gaps in a two-dimensional phononic crystal of pillars on a surface. Phys. Rev. B 81 (21), 214303.

Li, G.-Y., Xu, G., Zheng, Y., Cao, Y., 2018. Non-leaky modes and bandgaps of surface acoustic waves in wrinkled stiff-film/compliant-substrate bilayers. J. Mech. Phys. Solids 112, 239–252.

Liu, B., Chen, X., Cai, H., Mohammad Ali, M., Tian, X., Tao, L., Yang, Y., Ren, T., 2016. Surface acoustic wave devices for sensor applications. J. Semicond. 37 (2), 021001.

Lurie, K.A., 1997. Effective properties of smart elastic laminates and the screening phenomenon. Int. J. Solids Struct. 34 (13), 1633–1643.

Mace, B.R., Manconi, E., 2012. Wave motion and dispersion phenomena: Veering, locking and strong coupling effects. J. Acoust. Soc. Am. 131 (2), 1015–1028.

Mokhtari, A.A., Lu, Y., Srivastava, A., 2019. On the properties of phononic eigenvalue problems. J. Mech. Phys. Solids 131, 167–179.

Nassar, H., Chen, H., Norris, A.N., Haberman, M.R., Huang, G.L., 2017b. Non-reciprocal wave propagation in modulated elastic metamaterials. Proc. R. Soc. A 473 (2202), 20170188.

Nassar, H., Chen, H., Norris, A., Huang, G., 2017a. Non-reciprocal flexural wave propagation in a modulated metabeam. Extreme Mech. Lett. 15, 97–102.

Nassar, H., Xu, X., Norris, A., Huang, G., 2017c. Modulated phononic crystals: Non-reciprocal wave propagation and willis materials. J. Mech. Phys. Solids 101, 10–29.

Nassar, H., Yousefzadeh, B., Fleury, R., Ruzzene, M., Alù, A., Daraio, C., Norris, A.N., Huang, G., Haberman, M.R., 2020. Nonreciprocity in acoustic and elastic materials. Nat. Rev. Mater. 1–19.

Polewczyk, V., Dumesnil, K., Lacour, D., Moutaouekkil, M., Mjahed, H., Tiercelin, N., Petit Watelot, S., Mishra, H., Dusch, Y., Hage-Ali, S., Elmazria, O., Montaigne, F., Talbi, A., Bou Matar, O., Hehn, M., 2017. Unipolar and bipolar high-magnetic-field sensors based on surface acoustic wave resonators. Phys. Rev. A 8 (2), 024001.

Ruppel, C.C.W., 2017. Acoustic wave filter technology–a review. IEEE Trans. Ultrason. Ferroelectr. Freq. Control 64 (9), 1390–1400.

Swinteck, N., Matsuo, S., Runge, K., Vasseur, J.O., Lucas, P., Deymier, P.A., 2015. Bulk elastic waves with unidirectional backscattering-immune topological states in a time-dependent superlattice. J. Appl. Phys. 118 (6), 063103.

Trainiti, G., Ruzzene, M., 2016. Non-reciprocal elastic wave propagation in spatiotemporal periodic structures. New J. Phys. 18 (8), 083047.

Wallen, S.P., Haberman, M.R., 2019. Nonreciprocal wave phenomena in spring-mass chains with effective stiffness modulation induced by geometric nonlinearity. Phys. Rev. E 99 (1), 013001.

Wang, Y., Yousefzadeh, B., Chen, H., Nassar, H., Huang, G., Daraio, C., 2018. Observation of nonreciprocal wave propagation in a dynamic phononic lattice. Phys. Rev. Lett. 121 (19), 194301.

Wu, T.-T., Huang, Z.-G., Lin, S., 2004. Surface and bulk acoustic waves in two-dimensional phononic crystal consisting of materials with general anisotropy. Phys. Rev. B 69 (9), 094301.

Wu, T.-T., Huang, Z.-G., Tsai, T.-C., Wu, T.-C., 2008. Evidence of complete band gap and resonances in a plate with periodic stubbed surface. Appl. Phys. Lett. 93 (11), 111902.

Yi, K., Collet, M., Karkar, S., 2017. Frequency conversion induced by time-space modulated media. Phys. Rev. B 96 (10), 104110.

Yu, Z., Fan, S., 2009. Complete optical isolation created by indirect interband photonic transitions. Nat. Photon. 3 (2), 91–94.

Zanjani, M.B., Davoyan, A.R., Mahmoud, A.M., Engheta, N., Lukes, J.R., 2014. One-way phonon isolation in acoustic waveguides. Appl. Phys. Lett. 104 (8), 081905.

Zhu, R., Liu, X., Hu, G., Yuan, F., Huang, G., 2015. Microstructural designs of plate-type elastic metamaterial and their potential applications: a review. Int. J. Smart Nano Mater. 6 (1), 14–40.